

# Young stellar populations and star clusters in NGC 1705 <sup>1</sup>

F. Annibali<sup>2,3</sup>, M. Tosi<sup>4</sup>, M. Monelli<sup>5</sup>, M. Sirianni<sup>3,6</sup>, P. Montegriffo<sup>4</sup>, A. Aloisi<sup>3,6</sup>, L. Greggio<sup>2</sup>

<sup>2</sup> *INAF - Osservatorio Astronomico di Padova, Vicolo dell'Osservatorio 5, I-35122 Padova, Italy*

<sup>3</sup> *Space Telescope Science Institute, 3700 San Martin Drive, Baltimore, MD 21218*

<sup>4</sup> *INAF - Osservatorio Astronomico di Bologna, Via Ranzani 1, I-40127 Bologna, Italy*

<sup>5</sup> *Instituto de Astrofísica de Canarias, Calle Via Lactea, E38200 La Laguna, Espana*

<sup>6</sup> *On Assignment from the Space Telescope Division of the European Space Agency*

## ABSTRACT

We present HST photometry of the late-type dwarf galaxy NGC 1705 observed with the WFPC2 in the F380W and F439W bands and with the ACS/HRC in the F330W, F555W, and F814W broad-band filters. We cross-correlate these data with previous ones acquired with the WFPC2 in the F555W, F814W bands, and derive multiband Color-Magnitude diagrams (CMDs) of the cross-identified individual stars and candidate star clusters. For the central regions of the galaxy, where HST-NICMOS F110W and F160W photometry is also available, we present U, B, V, I, J, H CMDs of the 256 objects with magnitudes measured in all bands.

While our previous study based on F555W, F814W, F110W and F160W data allowed us to trace the star formation history of NGC 1705 back to a Hubble time, the new data provide a better insight on its recent evolution. With the method of the synthetic CMDs, we confirm the presence of two strong bursts of star formation (SF). The older of the two bursts (B1) occurred between  $\sim 10$  and 15 Myr ago, coeval to the age of the central SSC. The younger burst (B2) started  $\sim 3$  Myr ago, and it is still active. The stellar mass produced by B2 amounts to  $\sim 10^6 M_{\odot}$ , and it is a factor of  $\sim 3$  lower for B1. The interburst phase was likely characterized by a much lower level of star formation rather than by its complete cessation.

The two bursts show distinct spatial distributions: while B1 is centrally concentrated, B2 is more diffused, and presents ring and arc-like structures that remind of an expanding shell. This suggests a feedback mechanism, in which the expanding superbubble observed in NGC 1705, likely generated by the (10–15) Myr burst, triggered the current strong star formation activity.

The excellent spatial resolution of the HRC allowed us to reliably identify 12 star clusters (plus the SSC) in the central  $\sim 26'' \times 29''$  region of NGC 1705, 10 of which have photometry in all the UBVIJH bands. The comparison of the cluster photometry with the GALEV populations synthesis models provides ages from  $\approx 10$  Myr to  $\approx 1$  Gyr, and masses between  $\approx 10^4$  and  $10^5 M_{\odot}$ . The conspicuous cluster population in the central regions, with one super star cluster, one populous cluster and several regular ones, confirm the strong star forming activity of NGC 1705.

*Subject headings:* galaxies: evolution — galaxies: individual: NGC 1705 — galaxies: irregular — galaxies: dwarf — galaxies: stellar content

## 1. Introduction

NGC 1705 is a blue compact dwarf (BCD) galaxy, with two characteristics which make it extremely interesting: a) it shows the best doc-

<sup>1</sup>Based on observations with the NASA/ESA Hubble Space Telescope, obtained at the Space Telescope Science Institute, which is operated by AURA for NASA under contract NAS5-26555

umented proof of an ongoing galactic outflow (Meurer et al. 1992, hereafter MFDC; Heckman et al. 2001), and b) its nucleus hosts a luminous super star cluster (SSC) with estimated mass  $\sim 10^5 M_{\odot}$ , probably a proto-globular cluster only 10 Myr old (Melnick et al. 1985; O’Connell et al. 1994; Ho & Filippenko 1996). NGC 1705 is almost unaffected by intervening obscuring clouds and is not excessively crowded, in spite of a distance of 5.1 Mpc, as determined from the Tip of the Red Giant Branch (Tosi et al 2001, hereafter T01). This allows HST to resolve its individual stars down to fairly faint magnitudes, and makes it an ideal benchmark to study the evolution of BCDs, an important class of galaxies absent in the Local Group.

NGC 1705 ( $\alpha_{2000} = 04\ 54\ 15.2$ ,  $\delta_{2000} = -53\ 21\ 40$ ,  $l = 261.08$  and  $b = -38.74$ ) has been classified by MFDC as a BCD with a fairly continuous SF regime and an approximate oxygen abundance of  $12 + \log(\text{O}/\text{H}) \simeq 8.46$ . An oxygen abundance of 8.36 was derived by Storch-Bergmann, Calzetti & Kinney (1994) from UV, optical and near infrared spectra, while more recently Lee & Skillman (2004) have inferred more precise abundances from 16 HII regions, 5 of which had the electron temperature directly estimated from the  $[\text{OIII}]\lambda\ 4363$  line. The resulting oxygen abundance is  $8.21 \pm 0.05$ , as in the Small Magellanic Cloud. Lee & Skillman also measured the nitrogen abundance and found a  $(\text{N}/\text{O})_{\text{HII}} = -1.75 \pm 0.06$ , in agreement with the  $(\text{N}/\text{O})_{\text{HI}} = -1.70 \pm 0.4$  found by Heckman et al. (2001) and Aloisi et al. (2005) from FUSE observations of the neutral gas. This N/O abundance ratio is among the lowest values derived in late-type dwarfs and is difficult to explain in terms of galactic chemical evolution, unless strong galactic winds with enhanced nitrogen loss are assumed (Romano, Tosi & Matteucci 2006).

UV spectra acquired with HST (Heckman & Leitherer 1997) showed that nearly half of the optical/ultraviolet light is contributed by the young stellar population, and possibly by the central SSC which may also power the observed bipolar outflow. From the lack of spectral stellar wind features, Heckman & Leitherer suggested that the stars in the luminous SSC of NGC 1705 are not more massive than 10–30  $M_{\odot}$ . Ground-based work (e.g. Quillen et al. 1995) revealed the pres-

ence of a composite stellar population, with the older ( $\sim 1\text{--}10$  Gyr) field population defining the galaxy morphology. Our HST data (T01) confirmed this result showing that the stellar population in the inner central region is dominated by stars 10–15 Myr old (i.e. roughly coeval to the SSC), which are not present in intermediate and outer regions. Intermediate-age stars populate all the galaxy within about 700–800 pc from the SSC, while stars up to several Gyrs old are detected wherever crowding is not too severe (i.e. outwards of 200–300 pc from the SSC) and become increasingly dominating towards the outer regions.

In Annibali et al. (2003, hereafter A03) we applied the synthetic CMD method to the T01 CMDs to infer the star formation history (SFH) of 8 concentric regions of NGC 1705 and found that the data are consistent with a rather continuous Star Formation (SF) activity, started at least 5 Gyr ago, and recently overcome by a strong, centrally concentrated burst with an age between 15 and 10 Myr ago. This recent SF episode appears then coeval to the birth of the SSC and to the onset of the galactic wind. No (or very little) SF seems to have occurred in NGC 1705 between 10 and 3 Myr ago, possibly as a consequence of gas sweeping/heating by the strong wind, but then a new, even stronger burst appears to have started everywhere in the galaxy about 3 Myr ago. The latter result suggests that the gas must have been able to cool and fall down on a very short timescale.

To better study the young stellar populations in NGC 1705, we have observed the galaxy at shorter wavelengths, in the F380W and F439W filters, and derived the CMDs of the resolved stars. In this respect, this work is complementary to that presented by T01, where the F555W, F814W, F110W and F160W images allowed us to map more accurately the intermediate age and old populations. Observations of the central region were also performed in F330W, F555W and F814W with the ACS/HRC. These new data allow us to check the SFH inferred from the previous data by A03 and to study the properties of the star clusters in NGC1705.

The data are described in Sect.2, the properties of the candidate star clusters are presented in Sect.3, while the CMDs of the resolved individual stars are presented and analysed in Sect.4. The

SFH of the resolved stars is discussed in Sect.5, and the overall results are discussed and summarized in Sect.6.

## 2. Observations and Data Reduction

### 2.1. WFPC2 data

The F380W and F439W observations of NGC 1705 were part of a WFPC2 four-band program (GO-7506). The F555W and F814W images were successfully obtained in March 1999 (and have already been presented by T01), while the F380W and F439W ones could be successfully acquired in 2000 November 10–11. Contrary to the original planning, technical failures has prevented us to obtain the F380W and F439W images with the same telescope orientation as the F555W and F814W ones. The two orientations turned out to differ by 111 degrees from each other, implying that the WF fields overlap only partially, as shown in Fig.1.

The pointing was organized to follow a dither pattern with CR-split of 0.5. For the F439W images we have 4 different pointing positions, while for the F380W we have only two different positions. Two exposures at each dither position were also requested for an easier cosmic-ray removal. We thus have 8 images of 2,900 s each and one of 140 s in F439W, and 4 images of 500 s, 2 of 600 s and 1 of 140 s in F380W. The adoption of the dithering and CR-split techniques allows us to improve the background estimate, identify hot pixels and smooth local pixel to pixel variations from images taken at different dither points, and improve the image sampling.

For each filter the dithered frames, calibrated through the standard STScI pipeline procedure, were combined in a single, fully sampled image (with total exposure time 23,200 s in F439W and 3,200 s in F380W), using the software package *Drizzle* (Fruchter & Hook 1998). The effective pixel size in the resampled images corresponds to  $0''.023$  and  $0''.05$  for the PC and WFCs respectively. The PSF in the resulting *drizzled* images has a FWHM of  $\approx 3$  pixels in F380W and F439W for both the PC and the WFs. Fig.2 displays the final images, with superimposed both the WFPC2 fields of the previous F555W and F814W data and the isophotal line contours used in T01 to define the 8 concentric regions.

The *drizzled* frames have been analyzed with

StarFinder, the code developed for astrometry and photometry in crowded stellar fields described in detail by Diolaiti et al. (2000). With this code a numerical PSF template can be either directly extracted by modelling the stars observed in the frame or it can be simulated with Tiny Tim (Krist & Hook 1999). In this case we have inferred the PSF from the images by computing the median average of 10 suitable stars after correction for the local background and surrounding sources.

A provisional list of candidate single stars is created including all brightness peaks at  $5\sigma$  above the background, and is then correlated with the template PSF in order of decreasing flux. We considered a candidate as a real star only if the correlation coefficient (i.e. a measure of the similarity with the PSF) was greater than 0.7. From the analysis of many simulations, this value was in fact derived as the best representation of the boundary between real stars and spurious detections.

During the PSF fitting, the code progressively creates a virtual copy of the observed field as a smooth background emission with superimposed stellar sources. The stars are modeled as weighted shifted replicas of the PSF template and added one by one, in order of decreasing intensity. Photometry is performed on each individual star by using a sub-image of size comparable to the diameter of the first diffraction ring of the PSF. The local background is approximated by a bilinear surface, the underlying halos of brighter stars outside the fitting region are given by the synthetic image, and the brighter stars inside this region are represented as weighted shifted replicas of the PSF and re-fitted together with the analyzed star. The fainter candidate stars inside the fitting region are instead neglected at this point and are analyzed with the same strategy only in a further step. If the photometric fit is acceptable, the catalog and the synthetic image are updated with the new entry. For a better astrometric and photometric accuracy, all known sources are fitted again after examining and fitting all the candidate objects. The stars are then subtracted to search for possible lost objects, which are examined and fitted with the same procedure in the original frame. This step was iterated three times for each filter.

All the sources with extended profile or detected in the immediate neighborhood of the SSC were listed separately. The instrumental magni-

tude  $m_i$  of each object in each filter and detector was estimated via the PSF-fitting technique and then calibrated into the HST-VEGAMAG system following the standard procedure described by Holtzman et al. (1995a, 1995b) and the updated coefficients provided by Biretta et al. (2000):

$$m = m_i + C_{\text{ap}} + C_{\infty} + ZP_V + C_{\text{CTE}}$$

where, the aperture correction  $C_{\infty}$  is an offset of  $-0.10$  (irrespective of filter and detector) to convert the magnitude from the  $0''.5$  radius into a nominal infinite aperture;  $ZP_V$  are the zero points taken from Baggett et al. (1997);  $C_{\text{CTE}}$  is the correction for the *charge transfer efficiency* given by Whitmore, Heyer, & Casertano (1999).  $C_{\text{ap}}$  is the correction to convert the photometry performed in the adopted aperture to that in the conventional  $0''.5$  aperture. StarFinder actually provides the stellar flux already in an infinite aperture, but for sake of homogeneity with the standard calibration prescriptions, we have preferred to translate its measured fluxes into the classical  $0''.5$  aperture. In this case the correcting coefficients  $C_{\text{ap}}$  were derived directly from the same PSF templates adopted for the photometric reduction and turned out to be negligible. The F380W and the F439W catalogs, derived independently with the above procedure, were then cross-correlated and only the objects with a spatial offset smaller than 1 pixel were retained. This led to 2083 stars detected in both filters.

The central region of NGC 1705 was also observed in F110W and F160W with the HST-NIC2 camera (see T01 for details). There are 256 objects cross-identified in all the bands from the ultraviolet through the near-infrared, 10 of which candidate star clusters (see Sect. 2.3). The CMDs of these 256 objects are shown in Fig.3, where individual stars are represented by dots and candidate clusters by filled circles. The field of view of the NIC2 camera covers region 7, most of region 6 and a small fraction of region 5 (see Fig.2 in T01). Naturally, only the brightest stars are visible from the F380W through the F160W bands. By comparing the CMDs of Fig.3 with the stellar models, we see that the 256 stars are mostly on the MS, red super-giant phases, and a few are on the AGB.

Hereinafter, we will name U, B, V, I, J and H the  $m_{\text{F380W}}$ ,  $m_{\text{F439W}}$ ,  $m_{\text{F555W}}$ ,  $m_{\text{F814W}}$ ,  $m_{\text{F110W}}$ , and  $m_{\text{F160W}}$  magnitudes calibrated in the HST-Vegamag system.

## 2.2. Errors and incompleteness

To evaluate the degree of incompleteness and blending of our photometry at each mag level, and to derive a reliable estimate of the photometric errors, we have performed a series of artificial star experiments, following the procedure created by P.M. at the Bologna Observatory and described by T01. In summary, we recursively added artificial stars in random locations of the frames, by dividing the fields of view in grids of non-overlapping cells and positioning at most one star per cell in each run. Then, we repeated exactly the same procedure of PSF fitting and calibration applied to the actual data. The artificial stars were added with a magnitude distribution similar to the observed luminosity function (LF), but with more objects at the faint end to take into account that the empirical LF at the fainter mags is more likely to be affected by incompleteness. We added a few objects at a time, in order not to alter the field crowding conditions, repeating the process as many times as needed to total about 200,000 artificial stars. The same threshold and correlation selection criteria applied to the real stars, and described above, were also applied to the output catalogue of the artificial stars.

The completeness of our photometry at each magnitude level was computed as the ratio of the number of recovered artificial stars over the number of added ones (considering as recovered objects only those found within 0.5 pix of the given coordinates, satisfying the adopted selection criteria and with magnitudes differing from the input ones less than  $\pm 0.75$  mag). The resulting completeness levels in the B band are listed in Table 1 for the 8 galactic regions.

The difference between input and output magnitudes of the artificial stars represents a robust estimate of the actual photometric error to be associated to each magnitude bin. These errors are usually larger than those provided by the data reduction packages, especially towards the fainter magnitudes. They have the further advantage of providing a good characterization of the effects of blending affecting crowded field photometries. In Fig. 4 we show the results of our procedure for the F439W filter for each of the 8 concentric regions (regions with the same behavior are grouped together). The error distribution is skewed towards

positive values of the (input–output) mags of the recovered artificial stars: this is the signature of a significant blending at the fainter mags, since a star is recovered brighter when it overlaps another star in the image.

### 2.3. ACS/HRC data and the cluster sample

From the shape of the extended objects in the WFPC2 F555W and F814W images of NGC 1705, T01 suggested that 30 of them are likely candidate star clusters (17 plus the SSC in the PC field, 4 in the WF2, 5 in the WF3, and 3 in the WF4), while 42 are probably background galaxies. To obtain a safer cluster selection in the central region of NGC 1705, we used the High Resolution Channel (HRC) of the Advanced Camera for Surveys (ACS), whose excellent spatial resolution allows both a reliable identification of the star cluster population, and a study of its morphological properties.

The HRC/ACS observations were performed in August 2003 in the F330W (U), F555W (V), and F814W (I) broad-band filters (program GTO-9989). The exposures were taken with a 3-point dithering pattern in each filter. The total exposure times are 680 s in U, and 420 s in both V and I.

For each filter, we coadded with MULTIDRIZZLE (Koekemoer et al. 2002) the three dithered frames, calibrated through the most up-to-date version of the ACS calibration pipeline (CALACS), into a single resampled image with a  $0.02''$  pixel size, i.e.  $\approx 0.7$  times the original HRC pixel size. The field of view of each image is  $\approx 26 \times 29$  *arcsec*<sup>2</sup>. The MULTIDRIZZLE procedure also corrects the ACS images for geometric distortion and provides removal of cosmic rays and bad pixels.

PSF-fitting photometry with the DAOPHOT package (Stetson 1987) in the IRAF<sup>2</sup> environment was performed on the final drizzled images.

To derive the PSF, we selected  $\sim 30$  stars in each frame. The PSF was modeled with an analytic Moffat function plus additive corrections de-

rived from the residuals of the fit to the selected stars. The additive corrections include only first-order derivatives of the PSF with respect to the X and Y positions in the image. This procedure allows us to follow the first order spatial variation of the PSF in the ACS/HRC field of view.

A source catalog was created from the detections above  $4\sigma$  in the sum of the U, V and I images. Aperture photometry with PHOT, and then PSF-fitting photometry with the ALLSTAR package, were performed at the position of the detected sources in each band. The U,V and I catalogs were then cross-correlated, leading to  $\approx 3000$  objects with a measured magnitude in all the three bands simultaneously. To search for compact clusters, we selected objects with sizes larger than the PSF (*sharpness*  $>0.5$ ), and magnitudes brighter than  $m_{F814W} \lesssim 22$  in the final photometric catalog. By visually inspecting the selected objects in all the images, we recognized several background galaxies. We ended up with 12 candidate clusters in our images. The location in the HRC image of the selected candidate clusters is indicated in Figure 5.

Intrinsic sizes of the candidate clusters were derived using the ISHAPE task in BAOLAB (Larsen 1999). ISHAPE models a source as an analytical function convolved with the PSF of the image. For each object, ISHAPE starts from an initial value for the FWHM, ellipticity, and orientation. These parameters are then iteratively adjusted until the best fit between the observed profile and the model convolved with the PSF is obtained. We adopted a fitting radius of  $\approx 4 \times \text{FWHM}$  (PSF) in the ISHAPE procedure, corresponding to  $0.3''$  in the I image. We also tested different input analytical functions. A King (1962) profile with a concentration parameter  $c = 30$  provides the best fit to the data. The ISHAPE output includes the intrinsic shape parameters which provide the best match to the observed source profile, and a residual image. The intrinsic effective radius, averaged over the three bands, is listed for each cluster in Table 2. The derived intrinsic effective radius distribution is presented in Fig. 6.

We derived the magnitudes of the selected candidate clusters in U, B, V, I, J and H by performing aperture photometry with PHOT on the ACS/HRC, WFPC2 and NIC2 data. We first produced for each filter a subtracted image where we

<sup>2</sup>IRAF is distributed by the National Optical Astronomy Observatories, which are operated by AURA, Inc., under cooperative agreement with the National Science Foundation

removed all the stars around the candidate star clusters. Then we performed aperture photometry on the subtracted images at the cluster positions inside a radius  $R_e$ , given by the convolution of the cluster intrinsic effective radius  $r_e$  with the PSF. From the definition of effective radius, the total magnitude is  $m_{TOT} = m(r < R_e) - 0.75$ .

To test for systematics, we compared the photometry for all the objects in common between the HRC and the WFPC2 catalogues. The comparison was performed only in the F555W and F814W filters, because the F330W filter of the HRC data is significantly different from the F380W filter of the WFPC2 data. The cross-correlation provides  $\approx 3000$  stars common to the HRC and WFPC2 datasets. For a direct comparison, the HRC magnitudes were converted into the WFPC2 Vega-mag system applying the transformations provided in Table 25 of Sirianni et al (2005). The agreement between the HRC and WFPC2 photometries in the F555W filter is very good, with a  $\Delta(mag_{HRC} - mag_{WFPC2})$  distribution peaked around  $\sim 0$ . The comparison in the F814W filter is instead less satisfactory, with a small offset  $\Delta(mag_{HRC} - mag_{WFPC2}) \sim 0.06$ . We checked for possible problems in the data reduction process, but were unable to identify the source of this slight discrepancy. A possible cause for the observed systematics could be the use of two different photometric packages (Starfinder and Daophot) for the reduction the WFPC2 and HRC datasets. In fact, it has been shown that different photometric packages used on the same image can yield magnitude offsets up to  $\sim 0.05 - 0.1$  mag, especially when dealing with fields with severe crowding and variable background due to unresolved sources (e.g. Hill et al. (1998), Holtzman et al. (2006)).

We provide in Table 2 the cluster photometry inside  $R_e$  in the different filters: F330W (HRC), F380W, F439W, F555W, F814W (WFPC2), and F110W, F160W (NIC2). In this paper, we will use the WFPC2 and NIC2 photometry to derive the cluster ages and masses, for consistency with the star formation history derived from the WFPC2 and NIC2 photometry of the resolved stars.

### 3. Star clusters properties

From the analysis of the HRC/ACS data, we end up with 12 bona fide candidate clusters in

the central region of NGC 1705, in addition to the SSC. 10 of them have photometry in all the U,B,V,I,J and H bands.

The color-color diagrams (U–V vs V–I, and U–V vs J–H) are presented in Fig. 7. The data are compared with the GALEV models (Anders & Fritze-v. Alvensleben 2003) for different metallicities, and ages from 4 Myr to 10 Gyr. The models are based on the Padova isochrones (Bertelli et al. 1994). The adopted IMF has a Salpeter slope, between  $0.1 M_\odot$  and  $120 M_\odot$ . Fig. 7 shows that SSP models of different metallicities are strongly degenerate. For this reason we derive the cluster ages assuming a metallicity of  $Z = 0.004$ , which is consistent with the abundances of NGC 1705 HII regions and of the resolved stars of young and intermediate age (T01, A03). The relative color-color diagram is presented in Fig. 8, where we also show the effect of reddening on the  $Z = 0.004$  models.

The cluster ages were derived by minimizing the difference between models and data colors in all possible combinations (15 colors), according to a  $\chi^2$  criterion, varying the age (between 4 Myr and 10 Gyr), and the reddening (between  $E(B-V)=0$  and 1) of the models. Cluster masses were then estimated from the mass-to-light ratios of the best fitting models in the I band.

The results of the analysis are provided in Table 2, where we list the best-fitting ages, masses and  $E(B - V)$  values for the 12 candidate star clusters. Clusters #6 and #8 are not well constrained by the fit, which allows for solutions in the range 8–90 Myr, depending on the reddening. If we limit the fit to the bluer bands (U,B and V), the best fit yields ages of the order of 100 Myr, in combination with low reddening, for clusters #6 and #8. From Table 2 we notice that these clusters are the least massive of our sample, with masses of the order of  $10^4 M_\odot$  for the old-age solution, and masses as small as  $\sim 3 \times 10^3 M_\odot$  for the young age solution. Thus their red light is particularly prone to fluctuations on their evolved star populations, which could explain why the fit is poorly constrained.

The derived cluster age and mass distributions are shown in Fig. 9. The distribution was obtained by adopting for clusters #6 and #8 the oldest solutions of the full fit ( $\approx 80$  and 90 Myr, respectively). The 12 clusters span an age range

between  $\approx 10$  Myr and 1.4 Gyr, and masses between  $\approx 10^4$  and  $10^5 M_\odot$ . The age distribution appears peaked around  $\approx 100$  Myr, and there are few clusters  $\approx 1$  Gyr old. Cluster 1 is as young as  $\approx 16$  Myr. It is very compact ( $r_e \approx 1$  pc), has a mass of  $\approx 6 \times 10^4 M_\odot$ , and it is located at  $\approx 20$  pc from the central super star cluster. The two most massive clusters (cluster #12,  $\approx 7 \times 10^4 M_\odot$ , and cluster #9,  $\approx 10^5 M_\odot$ ) in our sample are  $\approx 1.2$  Gyr old.

Extragalactic young stellar clusters can be divided into three categories (e.g. Larsen & Richtler 2000, Billet, Hunter & Elmegreen 2002 and references therein), according to their luminosity: super star clusters [ $M_V \lesssim -10.5$ ], populous clusters [ $M_V \leq -8.5$  for  $(B-V)_0 \geq -0.4$  and  $M_V \leq -9.5$  for  $(B-V)_0 < -0.4$ ], and regular ones. From Table 2 one can see that the central region of NGC 1705 contains one SSC, one populous cluster (cluster #1) and several regular ones. Notice however that cluster #9 is actually more massive than cluster #1, although not formally consistent with the definition of populous cluster.

Billett, Hunter & Elmegreen (2002) have identified 15 clusters (plus the central SSC) in HST-WFPC2 images of NGC 1705 and discussed their properties. This galaxy stands out of their sample of 22 nearby late-type dwarfs for the highest cluster density, exceeded only by NGC 1569 (Hunter et al 2000): the cluster population of NGC 1569 versus NGC 1705 count respectively 45 viz 15 normal clusters, 3 viz 1 SSCs, and 10 vs 1 populous clusters. Billett et al. (2002) also noticed that, while in other galaxies the clusters are relatively separated, in NGC 1705 the majority of them are found surrounding the central SSC, in agreement with our results (see Figs.5 and 14). A similar distribution has been found for the clusters in NGC 1569, from optical data (Hunter et al. 2000), and from HST J and H images (Origlia et al. 2001). The bottom panel of our Fig. 14 shows that the clusters trace well the spatial distribution of the intermediate-age (50–1000 Myr) stars in NGC 1705. NGC 1705 and NGC 1569 are therefore similar exceptions among late-type dwarfs, and their cluster properties probably reflect their intense recent SF activity: NGC 1569 has a recent SF rate (SFR) higher than in any other late-type dwarf with resolved stellar populations studied so far (Greggio et al. 1998, Angeretti et al. 2005);

second ranks NGC 1705, with a recent SFR a factor of a few lower (e.g. A03, Tosi 2007). This confirms Larsen & Richtler (2000) suggestion of a direct correlation between the number and luminosity of young clusters and the SF activity of the hosting galaxies.

In the HRC field of view, we identify 7 clusters in common with the Billett et al. (2002) sample (our clusters # 3, 6, 7, 8, 10, 11, 12, corresponding respectively to their clusters # 12, 14, 13, 11, 10, 9, 7). Billett et al. (2002) determined the age for each cluster by comparing the integrated cluster photometry in B, V and I with the models of Leitherer et al (1999). For our clusters #11 and #12, they derive an age of 1 Gyr, consistent with our results. For clusters #6 and #8 they derive ages of 7 Myr, which are marginally consistent with our solutions in the range (8 – 90) Myr. For clusters #3, #7 and #10, instead, we derive ages of  $97_{-49}^{+8}$ ,  $101_{-60}^{+9}$ ,  $80_{-17}^{+9}$  Myr, which are fairly older than their ages of 7, 15, and 7 Myr, respectively. This discrepancy does not arise from the different photometry, not from the different procedure to account for the reddening (Billet et al. (2002) assume an intrinsic reddening of 0.05 plus a foreground reddening of  $\sim 0.045$ , which is close to the values that we derive for the three clusters). Likely, the discrepancy results from the use of different SSP models, based on different stellar tracks and on a different adopted metallicity (Billet et al (2002) assume  $Z=0.008$ ).

#### 4. The Colour-Magnitude Diagrams of the resolved stars

With the resolved stars observed with WFPC2 and measured with the StarFinder procedure described in the previous sections, we have constructed the CMDs of each of the 8 concentric regions displayed in Fig.2. The U vs U-B, B vs B-V and I vs V-I CMDs are shown in Fig. 10, where regions 3-4 and regions 0-1-2 have been grouped together for simplicity, since they present similar CMDs. The number of objects in the CMDs is indicated in each panel. These numbers do not represent the actual stellar density in each region, since they also depend on: i) camera spatial resolution (higher on the PC which covers the central regions), ii) completeness of the photometry (higher for increasing galactocentric distance), iii)

area of the region (larger for increasing distance), and iv) fraction of region covered by the two observing runs (smaller for increasing galactocentric distance). As shown in Fig.2, the overlap of  $U, B, V$  and  $I$  frames is complete only for regions 6 and 7, while, moving outwards, an increasing fraction of the other regions lacks observations from one of the two runs. Over the whole galaxy, only 4886 stars of the 40810 with F555W and F814W photometry, have also F439W (down to  $V \gtrsim 28$ ), and 2083 stars have both F380W and F439W (down to  $U \lesssim 26$ ).

For an immediate interpretation of the CMDs in terms of stellar populations, we have superimposed in the central and right panels of Fig.10 the Padova stellar evolution tracks with metallicity  $Z=0.004$  (Fagotto et al. 1994b), adopting from T01 a distance of 5.1 Mpc, i.e.  $(m-M)_0=28.54$ , and a reddening  $E(B-V)=0.045$ . It is apparent that our CMDs are populated with stars in all the evolutionary phases: main-sequence (MS), red supergiants, red giant branch (RGB) and asymptotic giant branch (AGB) stars.

Star with masses lower than  $2M_\odot$  are sampled on the RGB, which is wide enough to be consistent with an age range extending up to a Hubble time. Unfortunately, the well known age-metallicity degeneracy of the RGB prevents us to firmly establish whether the red edge of the RGB corresponds to metal poor stars as old as the Universe, or to more metal rich ones "only" a few Gyrs old. The RGB component is only visible on the  $(V, I)$  CMD, due to incompleteness at the shorter wavelengths, as one can realize from the plotted tracks. Indeed, the  $U$  and  $B$  images are too shallow to reveal the faint, old stars. This is the reason why the  $(U, B)$  and  $(B, V)$  CMDs of the outer regions contain so little stars: these bands virtually show only the gradient of the young population. In this respect, the  $U, U-B$  and  $B, B-V$  diagrams do confirm the existence of a young stellar population diffused over the whole galaxy, although more centrally concentrated, as usually found in late-type dwarfs.

Common to all color combinations, we notice that the depth of the CMDs is lowest in the central region: this is due to crowding. The magnitude difference between the faintest stars detected in region 7 and in region 0-1-2 amounts to  $\sim 3, 2$  and 1 mags in the  $I, B$  and  $U$  bands respectively.

Actually, the resolved bluest stars are all bright, (and young) and not strongly affected by crowding.

Taking all these effects into account, we can conclude that the old population can be homogeneously distributed all over the galaxy, although more easily measured in the more external, less crowded, regions, while the youngest population is more centrally concentrated, although present everywhere up to the galaxy outskirts.

T01 found that the  $I, V-I$  CMDs of regions 7, 6 and 5 present an excess of stars along the  $15M_\odot$  evolutionary track, i.e. with age  $\lesssim 15$  Myr. This peculiarity is confirmed in all bands, as shown in Fig.3 where the CMDs of the 256 objects measured in all the 6 UBVIJH bands are plotted together with the  $15M_\odot$  track by Fagotto (1994b). In Fig.10 we plot this track as a thick line: the excess of stars is apparent also in these CMDs, and confined to the central regions. This feature includes 20-25 stars (i.e. 10% of the plotted population) to the right of the blue plume, sometimes showing up as a horizontal stripe at the top of the stellar distribution (in the redder  $I$  and  $H$  CMDs), sometimes as a sequence increasingly faint towards redder colors (in the  $V$  and  $U$  CMDs). This "wind-cone" is well confined in all the CMDs by the evolutionary tracks of stars with  $20M_\odot$  and  $15M_\odot$ , and corresponds to objects 10–15 Myr old, born in the strong central burst identified by T01 and A03, and coeval to the SSC. The unambiguous evidence of the presence and confinement of the 25 stars in the "wind-cone" in all the CMDs of Fig.3 confirms that a very strong SF burst has started 15 Myr ago and has lasted only a few Myrs.

Fig. 3 also shows stars bluer than the "wind-cone", suggesting that younger stars exist. Many of these objects are fairly well fitted by the dotted-line in Fig.3, showing the evolutionary track of a  $60M_\odot$ . Since the lifetime of a  $60M_\odot$  is  $\sim 4$  Myr, the bluest stars of Fig.3 must be of that age or younger. This component (e.g. at  $B-V \leq -0.3$ ) is present in the CMDs in Fig. 10 as well, where we notice that it shows up all over the galaxy, out to Region 0-1-2.

## 5. Star formation history

The SFH of the resolved field population in NGC 1705 was derived for the 8 regions of increas-

ing galactocentric distance by A03, applying the method of synthetic CMDs described by Tosi et al. (1991) and Greggio et al. (1998). For each region, the SFH was modeled, looking for the best agreement between observed and simulated CMDs in the V and I bands, and between the corresponding luminosity functions. For an a posteriori consistency check, A03 also compared the near infrared (J, H) CMDs with synthetic ones obtained assuming the SFH derived from the V and I data. They showed that the agreement in the near infrared is quite good as well.

Here, we want to check whether the SFH derived by A03 from the (V, I) data is consistent also with the new data. To this purpose, we do not try to model *ex novo* the SFH to reproduce the (B, V) CMDs and LFs, but assume the SFH already derived by A03, and check how it compares with the observed B, B-V CMDs.

We briefly recall here that the synthetic CMDs are produced via Monte Carlo extractions of (mass, age) pairs for an assumed Initial Mass Function (IMF), SF law, and initial and final epochs of the SF activity. Each star is placed in the theoretical  $\log(L/L_{\odot})$ ,  $\log T_{eff}$  plane via interpolation on the Padova evolutionary tracks (Fagotto et al. 1994a and b). Luminosity and effective temperature are transformed into the HST-Vegamag photometric system adopting the Origlia & Leitherer (2000) conversion tables. Absolute magnitudes are converted into apparent ones by applying reddening and distance modulus, in this case  $E(B-V)=0.045$  and  $(m-M)_0=28.54$ .

Then a completeness test is applied in order to determine whether retaining or rejecting the synthetic star, based on the results of the artificial star tests on the actual photometric data. Since we performed the photometry independently in the B and V bands, and then correlated the catalogues (see Section 2), we require, in the simulations, that the synthetic stars pass the test in both photometric bands. Photometric errors are assigned on the basis of the distribution of the output-minus-input magnitudes of the artificial stars. These errors take into account the various instrumental and observational effects, as well as systematic uncertainties due to crowding (i.e. blend of fainter objects into an apparent brighter one).

The extraction of (mass, age) pairs is stopped when the number of stars populating the syn-

thetic CMD (or portions of it) equals the observed one. The solution to this procedure is not unique, and consists of several (SFH, IMF, metallicity, distance, reddening) combinations which are in agreement with the observed CMD morphologies and the luminosity functions for different color bins.

The synthetic CMDs are compared to the observed ones separately for regions 7, 6, 5, 3-4 and 0-1-2. It is important to recall that the B, B-V CMDs sample only the area of intersection between the U, B and V, I data-sets. In particular, while there is a good spatial overlap for the most central regions (7,6,5), sampled by the PC camera, the superposition for the more external regions, sampled by the WF cameras, is poorer. The U, B data sample only  $\sim 3/4$  and  $\sim 1/2$  of the areas covered by regions 3-4 and 0-1-2 in the V, I data, respectively. This implies that the SFH presented in A03 must be scaled by these factors before comparison with the observed B, B-V CMDs for regions 3-4 and 0-1-2. Of course this re-scaled SFR is an approximation, because it is possible that there are spatial variations in the intensity of the SF within the same region. Table 3 summarizes the SFH for the different regions of NGC1705. The table is the same as Table 6 in A03, except for the entries in regions 3-4 and 0-1-2, which have been scaled by 0.75 and 0.5, respectively, to account for the areas of overlap.

The synthetic B, B-V CMDs and LFs obtained assuming the SFH of Table 3 are presented in Fig. 11. It is apparent that there is a good agreement between the simulations and the data, also considering that we have not performed any fine-tuning. In particular, the comparison between the LFs is statistically meaningful, as they have been obtained through an average on several runs corresponding to the same SFH. This allows us to minimize random effects due to the small number of objects in the CMDs. Performing an average on several runs, we recover 493, 2483, 1693, 196 and 179 stars in the synthetic CMDs for regions 7-6-5-34 and 012, respectively. For the same regions, the number of observed stars is 525, 2704, 1925, 236 and 149. Thus, simulations and data agree within 10 % for regions 7-6-5 and within 20 % for regions 3-4 and 0-1-2.

In the simulations of Fig. 11, the objects present in the B, B-V CMDs are mainly young stars in the

MS or blue-loop phases. Stars older than  $\sim 1$  Gyr are barely detected in B, given the incompleteness of our data. This implies that the new data can provide a better insight on the recent evolution of NGC 1705, but not on its earlier phases, which were much better analysed with the V and I data by A03, with a lookback time of about 5 Gyr.

The CMDs of Fig. 11 shows that the SFH derived by A03 provides a good agreement with the new data. However, we performed additional simulations to better constrain and validate the SFH during the last 50 Myr. From Fig. 11, we notice that stars older than  $\sim 50$  Myr populate the CMD at  $B > 23.5$ . Thus we focus on the portion of the observed CMD brighter than  $B = 23.5$  to constrain the most recent SFH .

As a first check, we tested the need for a strong SF activity started  $\sim 3$  Myr ago (B2), as derived by A03. To this purpose we performed new simulations without B2. We obtained new synthetic CMDs adopting the SFH of A03, but suppressing the SF activity in the last 3 Myr; the stars of B2 were then re-distributed either between 10 and 15 Myr ago (this case is shown in Fig.12), or between 50 and 10 Myr ago. In both cases, the simulations severely underestimate the number of blue stars at  $22.5 < B < 23.5$ , and thus confirm the need for a strong SF activity started only few Myrs ago and still ongoing. Only in the outermost regions 0-1-2 the significance of this result may be questioned: too few stars are measured in B and V in the periphery to clearly distinguish between the two scenarios.

We notice that despite the overall good agreement with the data, the simulations in Fig. 11 slightly underproduce the stars in the brightest magnitude bins ( $B < 21$ ). A comparison with the stellar evolution tracks indicate that these objects are likely very massive stars that started to evolve out of the MS phase after  $\approx 3$  Myr since their birth, and that have a lifetime  $\lesssim 10$  Myr. Thus, we tested the need for an interruption in the SF activity between burst B1 and burst B2 as derived by A03. As a first check, we simulated the total-ity of the stars produced in the two bursts within a single episode started 15 Myr ago and still ongoing. This translates into rates of  $5.3 \times 10^{-2}$ ,  $3.5 \times 10^{-2}$ , and  $6.3 \times 10^{-3} M_{\odot} \text{ yr}^{-1}$  for Regions 7, 6 and 5 , respectively. The synthetic CMDs and LFs for this scenario, shown in Fig.13, are

strongly inconsistent with the data for Regions 7 and 6, since they cause an overproduction of very luminous blue stars. For example, in Reg. 7 the simulation provides  $\approx 90$  stars with  $B - V < 0.4$  and  $B < 22$  against 35 stars observed, and 6 stars with  $B < 20.5$  against 0 observed. In Reg 5, instead, the data are consistent with a continuous episode from 15 Myr to now at a rate of  $6 \times 10^{-3} M_{\odot} \text{ yr}^{-1}$ .

Because of the small statistics at  $B < 21$ , we did not attempt to derive a best fit SFR between B1 and B2, but rather tried to derive an upper limit. To this purpose, we simulated new CMDs where we forced the SFR between B1 and B2 to assume increasing values from  $10^{-4}$  to  $10^{-1} M_{\odot} \text{ yr}^{-1}$ . The rates of the other episodes were re-scaled from our best-fit SFH in order to reproduce the number of observed stars in each region. Then, we compared the data with the simulations focusing on the brightest ( $B < 21$ ) portion of the CMD, sampling the post-MS phase of massive ( $M > 20 M_{\odot}$ ) stars with ages between 3 and 10 Myr. To derive a conservative upper limit for the interburst rate, we required statistical consistency at a 95 % confidence level between the simulated and observed counts at  $B < 20.5$  and  $20.5 < B < 21$ . This provides an upper limit of  $\approx 10^{-2} M_{\odot} \text{ yr}^{-1}$  for both Regions 7 and 6. For instance, a rate of  $10^{-2} M_{\odot} \text{ yr}^{-1}$  produces, over 10 runs, an average of  $\sim 3.5$  simulated counts at  $B < 20.5$  in Reg. 7, against 0 counts observed. The extracted counts follow a Poisson distribution, and are consistent with the observed counts with a probability  $< 5$  %. The derived upper limit of  $10^{-2} M_{\odot} \text{ yr}^{-1}$  is a factor  $\approx 4$  and 16 lower than the rates derived in Reg. 7 for B1 and B2, respectively, and a factor  $\approx 2$  and 10 lower than the rates of B1 and B2 in Reg. 6. Our results indicate that the interburst state was more likely characterized by a lower level of star formation rather than by its complete cessation.

The occurrence of the two recent bursts, separated by only few Myrs, is particularly intriguing since it suggests a feedback mechanism as the trigger for the more recent episode. To get insight into this possible scenario, we investigated the spatial distribution of the stars generated during B1 and B2 in the PC field. With the help of the synthetic CMD simulations performed, we selected in the observed CMD stars younger than  $\approx 5$  Myr, be-

longing to B2 ( $(B-V), (V-I) \lesssim 0.3, 22.5 < B < 23.5, 22.5 < I < 24$ ) and stars with ages (10-15) Myr, generated during B1 ( $I \lesssim 21$ ), and plotted their spatial distribution in Fig.14. Intermediate-age ((50-1000) Myr) stars and candidate clusters are plotted as well for comparison. Fig.14 shows that while B1 is confined to the most central region, the current burst B2 is more extended, and presents some ring/arc - like structures which remind of an expanding shell. This suggests a scenario in which SF occurred 10-15 Myr ago in the very center of NGC 1705; then multiple supernovae explosions generated a strong galactic wind and a superbubble that, expanding, shocked and compressed the surrounding ISM; when the gas cooled after few Myrs, new more external SF occurred in the regions shocked by the superbubble (see also Burkert 2004).

## 6. Discussion and conclusions

With the new data presented here (WFPC2 imaging in U and B, HRC imaging in U, V and I) we have completed our multiband HST photometric analysis of NGC 1705, from the ultraviolet to the near infrared. Since the new data are mostly sensitive to bright blue stars, they provide a better insight on the recent evolution of NGC 1705, but not on its old SFH. Epochs older than few hundreds Myr were much better constrained from the analysis of the V, I, J and H data by A03, who concluded that NGC 1705 was already forming stars several Gyrs ago. Between  $\approx 1$  Gyr and 50 Myr ago, they also derived a "fluctuating" star formation of moderate strength, excluding long interruption in the SF activity.

In this paper, we applied the method of the synthetic CMDs to the new data to better constrain the SFH of NGC 1705 in the last  $\sim 50$  Myr. We confirm the presence of two strong young bursts, as derived by A03 from longer wavelength data. The older of the two bursts (B1) occurred between  $\sim 10$  and 15 Myr ago, and is coeval to the age of the central SSC. The younger burst (B2) started  $\sim 3$  Myr ago, and it is still active. The stellar mass produced by B2 amounts to  $\sim 10^6 M_{\odot}$ , and it is a factor of  $\sim 3$  lower for B1. The new data allowed us also to test for possible SF activity between the two bursts. The comparison of the data with detailed simulations shows evidence for a drop of

the rate in the interburst interval rather than for a complete cessation of the activity. We derived an upper limit of  $10^{-2} M_{\odot} \text{ yr}^{-1}$  for the rate allowed between the two bursts, which is a factor  $\sim 4$  and 16 lower than the rates of B1 and B2 in the center of NGC 1705, respectively. This result agrees with the conclusions of Lee et al. (2009) based on the analysis of the  $H\alpha$  component of the 11HUGS Survey. The authors showed that the complete cessation of star formation generally does not occur in irregular galaxies, and is not characteristic of the interburst phase.

The two bursts in NGC 1705 appear well separated in space: while B1 is centrally concentrated, B2 occurs all over the galaxy, and presents ring and arc-like structures reminiscent of an expanding shell. These results suggest a feedback scenario in which the most recent burst was triggered by the expanding superbubble generated during the previous (10–15) Myr burst. Hydrodynamical simulations (Burkert, private communication) show that a few Myr interval between the two bursts is sufficient for the shocked gas to cool down and allow the formation of new stars.

The excellent spatial resolution of the HRC allowed us to reliably identify 12 star clusters (plus the SSC) in the central  $\sim 26'' \times 29''$  region of NGC 1705, and to study their morphological properties. The clusters have intrinsic effective radii from  $\sim 1$  to 6 pc. From the comparison of their integrated WFPC2/NIC2 UBVIJH photometry with the GALEV population synthesis models, we derive cluster ages from  $\approx 10$  Myr to  $\approx 1$  Gyr, and masses between  $\approx 10^4$  and  $10^5 M_{\odot}$ .

Some of the properties derived for NGC 1705 in A03 and in this work are similar to those inferred for all the other late-type dwarfs whose resolved stellar populations have been studied so far, either inside or outside the Local Group (for a summary, see e.g. Tosi 2007). All of them have been shown to be already forming stars at the lookback time reached by the photometry, both irregulars (see e.g. Aparicio, Gallart & Bertelli 1997 for Pegasus, Dolphin et al. 2001 for the SMC, Smecker-Hane et al. 2002 for the LMC, Clementini et al. 2003 for NGC 6822, Dolphin et al. 2003 for Sextans A, Skillman et al. 2003 for IC 1613, Grocholski et al. 2008 for NGC 1569, Cole et al. 2007 for Leo A) and BCDs (see e.g. Lynds et al. 1998 for VIIZw403, Schulte-Ladbeck et al. 2000 for Mrk 178,

Schulte-Ladbeck et al. 2001 for IZw36, Aloisi et al. 2005 for SBS1415+437, Aloisi et al. 1999, Ostlin 2000 and Aloisi et al. 2007 for IZw18). In other words, no galaxy has been found yet with evidence of having started to form stars only recently, not even the most metal-poor ones, IZw18 and SBS1415+437.

Also common to all the late-type dwarfs studied by means of the CMDs of their resolved stellar populations is the result that their SFH has been fairly continuous, with fluctuations in the SFR and the possibility of short quiescent phases (*gasping* SF regime, Marconi et al. 1995). What makes NGC 1705 outstanding is the strength of its recent SF episodes, comparable only to that of the other very active and windy dwarf irregular NGC 1569. It is interesting to emphasize that the strength of the SF activity does not appear to be related to the morphological classification of the galaxy: all the other BCDs with inferred SFH have SFR comparable to those of nearby dwarf irregulars (i.e. of the order of  $0.005 M_{\odot} \text{ yr}^{-1} \text{ kpc}^{-2}$ , while the recent burst in NGC 1705 has a SFR density of  $1 M_{\odot} \text{ yr}^{-1} \text{ kpc}^{-2}$  and that in NGC 1569 has  $> 4 M_{\odot} \text{ yr}^{-1} \text{ kpc}^{-2}$ ). In this respect dwarf irregulars and BCDs do not differ from each other. One may actually think, on the basis of the current sample, that BCDs are simply dwarf irregulars with a recent SF activity strong enough to let them be discovered in spite of the distance and the relative faintness.

NGC 1705 and NGC 1569, in spite of being differently classified, have many common features, in addition to (or because of) the strength of their recent SF activity: they both show observational evidence of galactic winds, they both host SSCs (1 NGC 1705, and 3, possibly 6, depending on the definition, NGC 1569), and they both contain a large number of star clusters (see also Billett et al. 2002).

Galaxy evolution models (Romano et al. 2006), computed adopting the SFH inferred from the CMDs of the resolved stars, show that both in NGC 1705 and NGC 1569 the strong SF activity triggers violent galactic winds powered by Supernova explosions. The predicted winds eject total masses of gas consistent with the observational estimates (MFDC, Martin, Kobulnicky & Heckman 2002). They remove efficiently from the galaxies the metals produced by the Supernovae but only

tiny fractions of the interstellar medium, as expected on the basis of both observations and hydrodynamical models (e.g. De Young & Gallagher 1990, D’Ercole & Brighenti 1999, Mac Low & Ferrara 1999, Martin et al. 2002, Recchi et al. 2006). These differential winds appear to be the only viable explanation to reconcile the strength of the recent SF activity, and the long duration of the previous one, with the current low metallicities and high gas content observed in both galaxies.

The presence of one SSC, one populous cluster and several regular star clusters in the central regions of NGC 1705 confirm its unusually high activity, surpassed only by the extreme one of NGC 1569. The fairly long age range of these clusters also indicates a prolonged star formation activity. Once again, NGC 1569 and NGC 1705 look fairly similar to each other in their star and cluster formation efficiencies higher than in other late-type dwarfs.

We are grateful to Luca Angeretti for his support on the synthetic CMD code and Livia Origlia for providing the photometric conversion tables to the Vegamag system. We thank A. Burkert, R. P. van der Marel and U. Fritze-v. for useful discussions and P. Anders for providing the GALEV models. We thank the anonymous referee for the very useful comments to improve the paper. We acknowledge financial contribution from INAF through PRIN-2005 and ASI-INAF through contract I/016/07/0.

## REFERENCES

- Aloisi, A., Annibali, F., Mack, J., Tosi, M., van der Marel, R.P., Clementini, G., Contreras, R.A., Fiorentino, G., et al. 2007, IAU Symp. 241, 310
- Aloisi, A., Heckman, T.M., Hoopes, C.G., Leitherer, C., Savaglio, S., Sembach, K.R., 2005 in Starbursts: from 30 Doradus to Lyman Break galaxies; R. de Grijs, R.M. Gonzales-Delgado eds (Springer, Dordrecht), p.P2
- Aloisi, A., Tosi, M., & Greggio, L. 1999, AJ, 118, 302
- Aloisi, A., van der Marel, R.P., Mack, J., Leitherer, C., Sirianni, M., & Tosi, M. 2005, ApJ, 631, L45

- Anders, P., & Fritze-v. Alvensleben, U. 2003, A&A, 401, 1063
- Angeretti, L., Tosi, M., Greggio, L., Sabbi, E., Aloisi, A., & Leitherer, C. 2005, AJ, 129, 2203
- Annibali, F., Greggio, L., Tosi, M., Aloisi, A., & Leitherer, C., 2003, AJ, 126, 2752 (A03)
- Aparicio, A., Gallart, C., & Bertelli, G., 1997a, AJ, 114, 669
- Baggett, S., Casertano, S., Gonzaga, S., & Ritchie, C. 1997, ISR WFPC2 97-10
- Bertelli, G., Bressan, A., Chiosi, C., Fagotto, F., & Nasi, E. 1994, A&AS, 106, 275
- Billett, O.H., Hunter, D.A., & Elmegreen, B.G. 2002, AJ, 123, 1454
- Biretta, J.A., et al. 2000, WFPC2 Instrument Handbook, Version 5.0 (Baltimore: STScI)
- Burkert, A. 2004, The Formation and Evolution of Massive Young Star Clusters, 322, 489
- Clementini, G., Held, E.V., Baldacci, L., & Rizzi, L. 2003, ApJ, 588, L85
- Cole, A.A., et al. 2007, ApJ, 659, L20
- D'Ercole, A., & Brighenti, F. 1999, MNRAS, 309, 941
- De Young, D.S., &gallagher, J.S. 1990, ApJ, 356, L15
- Diolaïti, E., Bendinelli, O., Bonaccini, D., Close, L., Currie, D., Parmeggiani, G., 2000, A&AS, 147, 335
- Dolphin, A.E., Saha, A., Skillman, E.D., et al. 2003, AJ, 126, 187
- Dolphin, A.E., Walker, A.R., Hodge, P.W., Mateo, M., Olszewski, E.W., Schommer, R.A., Suntzeff, N.B.. 2001, ApJ, 562, 303
- Fagotto, F., Bressan, A., Bertelli, G., & Chiosi, C. 1994a, A&AS, 104, 365
- Fagotto, F., Bressan, A., Bertelli, G., & Chiosi, C. 1994b, A&AS, 105, 29
- Fruchter, A.S., & Hook, R.N. 1998, PASP, astro-ph/9808087
- Greggio, L., Tosi, M., Clampin, M., De Marchi, G., Leitherer, C., Nota, A., & Sirianni, M. 1998, ApJ, 504, 725
- Grocholski, A. J., Aloisi, A., van der Marel, R. P., Mack, J., Annibali, F., Angeretti, L., Greggio, L., Held, E. V., Romano, D., Sirianni, M., Tosi, M., 2008, ApJL, 686, L79
- Heckman, T.M., & Leitherer, C. 1997, AJ, 114, 69
- Heckman, T.M., Sembach, K.R., Meurer, G.R., Strickland, D.K., Martin, C.L., Calzetti, D., & Leitherer, C., 2001, ApJ, 554, 1021
- Hill, J.R. et al. 1998, ApJ, 496, 648
- Ho, L.C., & Filippenko, A.V. 1996, ApJ, 466, L83
- Holtzman, J.A., Burrows, C., Casertano, S., Hester, J., Trauger, J., Watson, A., & Worthey, G. 1995a, PASP, 107, 1065
- Holtzman, J.A., et al. 1995b, PASP, 107, 156
- Holtzman, J. A., Afonso, C., Dolphin, A. 2006, ApJS, 166, 534
- Hunter, D.A., O'Connell, R.W., Gallagher, J.S. & Smecker-Hane, T.A. 2000, AJ, 120, 2383
- King, I. 1962, AJ, 67, 274
- Koekemoer, A. M., Fruchter, A. S., Hook, R. N., & Hack, W. 2002, The 2002 HST Calibration Workshop, 2002. Edited by Santiago Arribas, Anton Koekemoer, and Brad Whitmore. Baltimore, MD: Space Telescope Science Institute, 2002., p.337, 337
- Krist, J., & Hook, R., 1999, Tiny Tim User Manual Version 5.0, (Baltimore: STScI)
- Larsen, S. S. 1999, A&AS, 139, 393
- Larsen, S.S. & Richtler, T. 2000, A&A, 354, 836
- Lee, H., & Skillman, E.D. 2004, ApJ, 614, 698
- Lee, J. C., Kennicutt, R. C., José G. Funes, S. J., Sakai, S., & Akiyama, S. 2009, ApJ, 692, 1305
- Leitherer, C., et al. 1999, ApJS, 123, 3
- Lynds, R., Tolstoy, E., O'Neil, E.J.Jr., & Hunter, D.A. 1998, AJ116, 146
- Mac Low, M.-M. & Ferrara, A. 1999, ApJ, 513, 142
- Marconi, G., Tosi, M., Greggio, L., & Focardi, P. 1995, AJ, 109, 173
- Martin, C.L., Kobulnicky, H.A., & Heckman, T.M. 2002, ApJ, 574, 663
- Melnick, J., Moles, M., & Terlevich, R. 1985, A&A, 149, L24
- Meurer, G.R, Freeman, K.C., Dopita, M.A., Cacciari, C. 1992, AJ, 103, 60 (MFDC)

- O'Connell, R.W., Gallagher, J.S., & Hunter, D.A. 1994, *ApJ*, 433, 65
- Origlia, L. & Leitherer, C. 2000, *AJ*, 119, 2018
- Origlia, L., Leitherer, C., Aloisi, A., Greggio, L., Tosi, M. 2001, *AJ*, 122, 815
- Ostlin, G. 2000, *ApJ*, 535, L99
- Quillen, A.C., Ramirez, S.V., & Frogel, J.A., 1995, *AJ*, 110, 205
- Recchi, S., Hensler, G., Angeretti, L. & Matteucci, F. *A&A*, 445, 875
- Romano, D., Tosi, M., & Matteucci, F. 2006 *MNRAS*, 365, 759
- Sirianni, M., Meurer, G., Homeier, N., Clampin, M., Kimble, R., & The ACS Science Team 2005, *Starbursts: From 30 Doradus to Lyman Break Galaxies*, 329, 41
- Schulte-Ladbeck, R.E., Hopp, U., Greggio, L. & Crone, M.M. 2000 *AJ*, 120, 1713
- Schulte-Ladbeck, R.E., Hopp, U., Greggio, L., Crone, M.M., & Drozdovsky, I.O. 2001, *AJ*, 121, 3007
- Skillman, E.D., Tolstoy, E., Cole, A.A, Dolphin, A.E., Saha, A., Gallagher, J.S., Dohm-Palmer, R.C., Mateo, M. 2003, *ApJ*, 596, 253
- Smecker-Hane, T.A., Cole, A.A., Gallagher, J.S., & Stetson, P.B. 2002, *ApJ*, 566, 239
- Stetson, P. B. 1987, *PASP*, 99, 191
- Storchi-Bergmann, T., Calzetti, D. & Kinney, A. 1994, *ApJ*429, 572
- Tosi, M. 2007, in *From Stars to Galaxies*, A.Vallenari, R.Tantalo, L.Portinari & A.Moretto eds, *ASP Conf.Ser.*, 374, p. 221
- Tosi, M., Greggio, L., Marconi, G., & Focardi, P. 1991, *AJ*, 102, 951
- Tosi, M., Sabbi, E., Bellazzini, M., Aloisi, A., Greggio, L., Leitherer, C., Montegriffo, P., 2001, *AJ*, 123, 1271, T01
- Whitmore, B., Heyer, I., & Casertano, S. 1999, *PASP*, 111, 1559

TABLE 1

B-BAND COMPLETENESS LEVELS IN EACH REGION FROM THE ARTIFICIAL STAR TESTS.

mag	$c_7$	$c_6$	$c_5$	$c_4$	$c_3$	$c_2$	$c_1$	$c_0$
20	1.00	1.00	1.00	1.00	1.00	1.00	1.00	1.00
22	0.94	0.94	0.82	1.00	1.00	1.00	1.00	1.00
24	0.64	0.82	0.89	0.54	0.54	0.97	0.97	0.96
26	0.13	0.20	0.60	0.61	0.78	0.92	0.91	0.84
28	0.00	0.00	0.00	0.02	0.09	0.12	0.11	0.10

TABLE 2  
NGC 1705 CLUSTER PROPERTIES

Cluster	$r_e$ (")	$r_e$ (pc) <sup>a</sup>	$M_{F555W}^a$	$m_{F330W}^b$	$m_{F380W}^b$	$m_{F439W}^b$	$m_{F555W}^b$	$m_{F814W}^b$	$m_{F110W}^b$	$m_{F160W}^b$	E(B - V)	Age(Myr)	Mass ( $10^4 M_\odot$ )
SSC <sup>c</sup>	0.08	1.98	-13.8	13.6	-	-	14.9	15.0	-	-	0.06	12	59
1	0.04	0.99	-9.57	17.77	18.72	19.01	19.08	18.89	18.68	18.18	0.0	$16_{-2}^{+2}$	$6.15_{-1.3}^{+0.1}$
2	0.13	3.21	-7.53	21.23	21.61	21.64	21.43	20.79	20.51	19.83	0.1	$53_{-4}^{+1}$	$1.74_{-0.1}^{+0.1}$
3	0.26	6.43	-7.22	21.93	21.83	21.74	21.58	21.18	-	-	0.05	$97_{-49}^{+8}$	$1.69_{-0.8}^{+0.1}$
4	0.19	4.7	-7.54	21.29	21.60	21.62	21.42	20.88	-	-	0.1	$101_{-14}^{+11}$	$2.41_{-0.2}^{+0.1}$
5	0.15	3.71	-7.35	21.61	21.66	21.62	21.30	20.67	20.01	19.19	0.0	$356_{-73}^{+202}$	$3.73_{-0.5}^{+1.7}$
6*	0.175	4.33	-6.66	21.89	22.20	22.23	21.99	21.60	21.52	21.16	$\leq 0.15$	8 - 80	0.3 - 1
7	0.22	5.44	-6.84	22.26	22.41	22.38	22.12	21.57	21.31	20.60	0.1	$101_{-60}^{+9}$	$1.28_{-0.6}^{+0.1}$
8*	0.15	3.71	-6.85	21.84	22.01	22.02	21.80	21.43	21.28	20.81	$\leq 0.2$	8 - 90	0.3 - 1.2
9	0.1	2.47	-7.57	21.84	21.85	21.72	21.08	20.21	19.71	18.95	0.0	$1191_{-210}^{+209}$	$9.39_{-1.3}^{+0.7}$
10	0.26	6.43	-7.22	21.59	21.76	21.77	21.55	21.09	20.76	20.22	0.1	$80_{-17}^{+9}$	$1.94_{-0.2}^{+0.1}$
11	0.16	3.95	-6.31	23.08	23.21	23.05	22.34	21.33	20.84	20.14	0.0	$1427_{-371}^{+705}$	$3.86_{-0.5}^{+2.2}$
12	0.21	5.19	-7.19	22.30	22.33	22.24	21.46	20.52	20.06	19.36	0.0	$1260_{-317}^{+410}$	$6.94_{-0.2}^{+2.7}$

<sup>a</sup> Correcting for  $(m - M)_0 = 28.54$ , corresponding to a distance of 5.1 Mpc (Tosi et al. 2001), for a galactic reddening E(B-V)=0.035, and for the intrinsic E(B-V) listed in this Table.

<sup>b</sup> Apparent magnitudes measured within a radius  $R = r_e * PSF$

<sup>c</sup> From Sirianni et al. (2005)

\* For these clusters the fit is problematic and provides a wide range of solutions.

TABLE 3  
AVERAGE SFRs\* AT VARIOUS EPOCHS

Region	Area ( $kpc^2$ )	SFR ( $M_{\odot}yr^{-1}$ )					
		(0-3) Myr	(3-10) Myr	(10-15) Myr	(15-50) Myr	(50-1000) Myr	(1-5) Gyr
7	0.017	0.16	–	0.044	–	$4.3 \times 10^{-3}$	?
6	0.13	0.11	–	0.022	0.005	0.024	$1.3 \times 10^{-2}$
5	0.35	0.032	–	$2.1 \times 10^{-3}$	$2.7 \times 10^{-3}$	0.022	$1.6 \times 10^{-2}$
3-4	0.64	0.005	–	–	–	$5.5 \times 10^{-3}$	$0.75 \times 10^{-2}$
0-1-2	5.6	0.0025	–	–	–	$2.5 \times 10^{-4}$	$0.85 \times 10^{-2}$
total	6.7	0.31	–	$6.8 \times 10^{-2}$	$7.7 \times 10^{-3}$	$5.6 \times 10^{-2}$	$4.5 \times 10^{-2}$

\* The rates are those derived in A03 and re-scaled to the area of overlap between the (V, I) and (U,B) datasets.

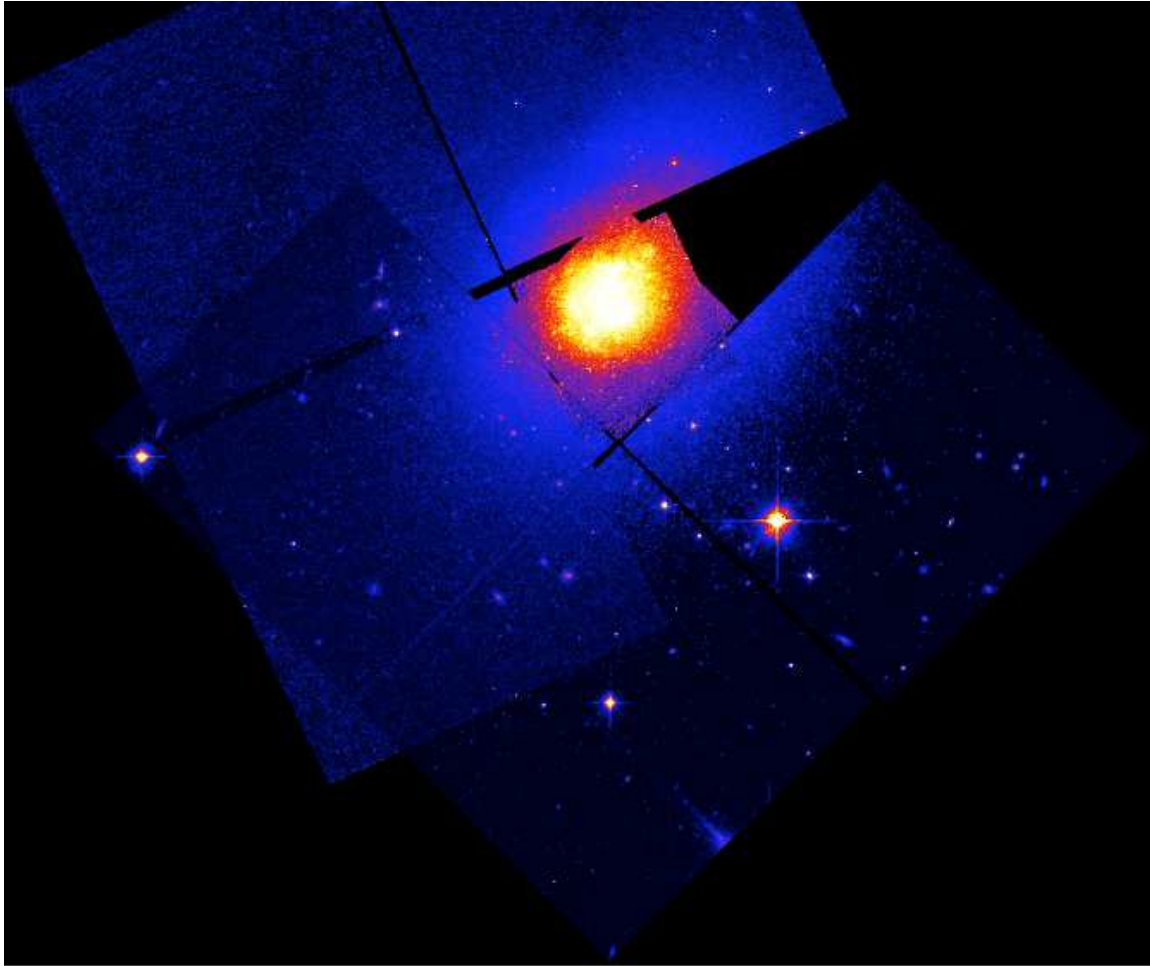


Fig. 1.— WFPC2 images of NGC 1705 in F439W and F814W. The different orientations of the two observing runs unfortunately prevent the images to completely overlap as planned. North is up and East is to the left.

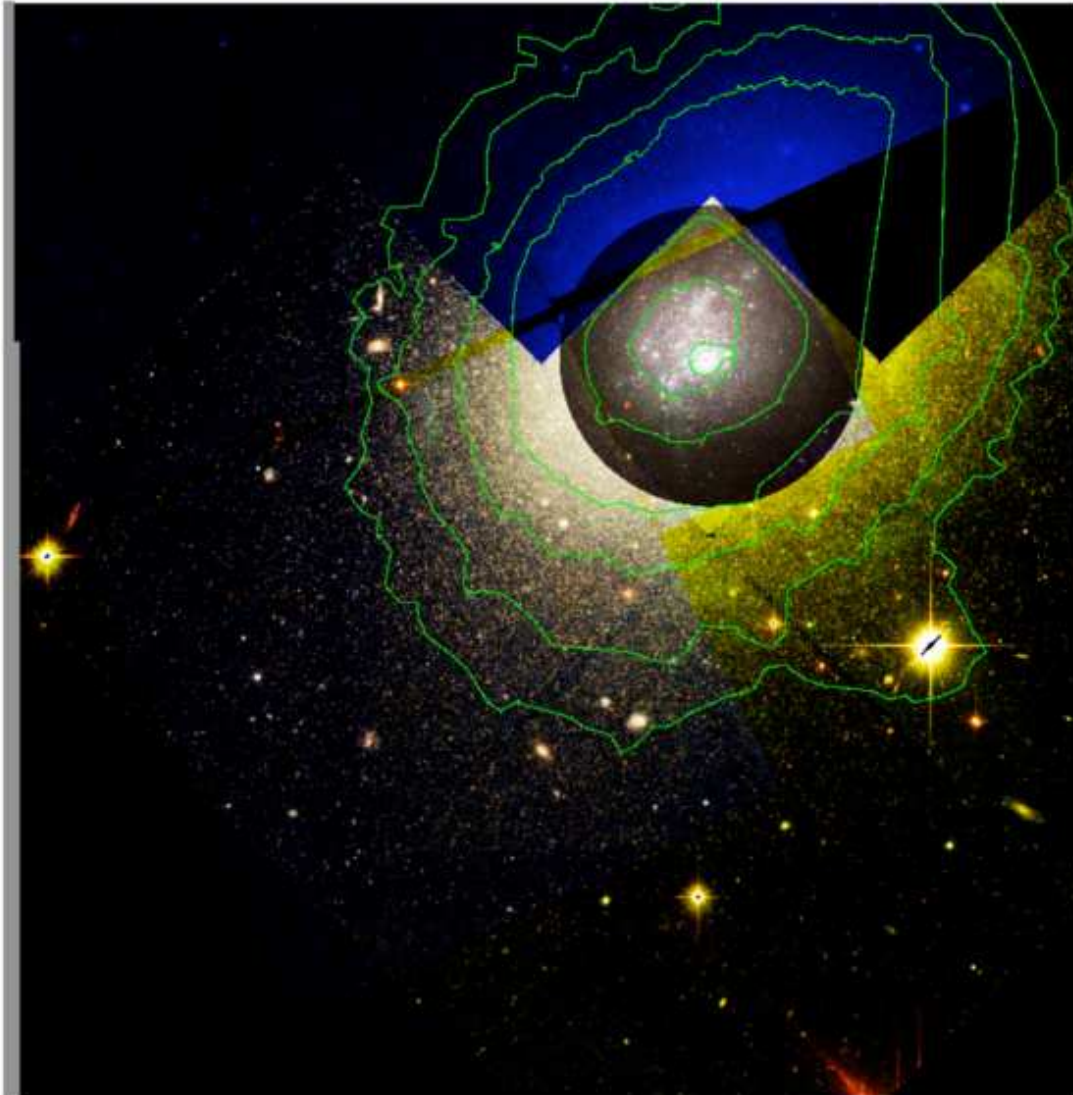


Fig. 2.— True color WFPC2 image of the regions of NGC 1705 where the F380W, F439W, F555W, and F814W fields overlap. In the rest of the fields either F380W and F439W are available (blue portions of the figure), or the F555W and F814W (yellowish portions). Overimposed (in green) are the isophotal contour levels adopted by TO01 to define 8 roughly concentric regions (see text for details).

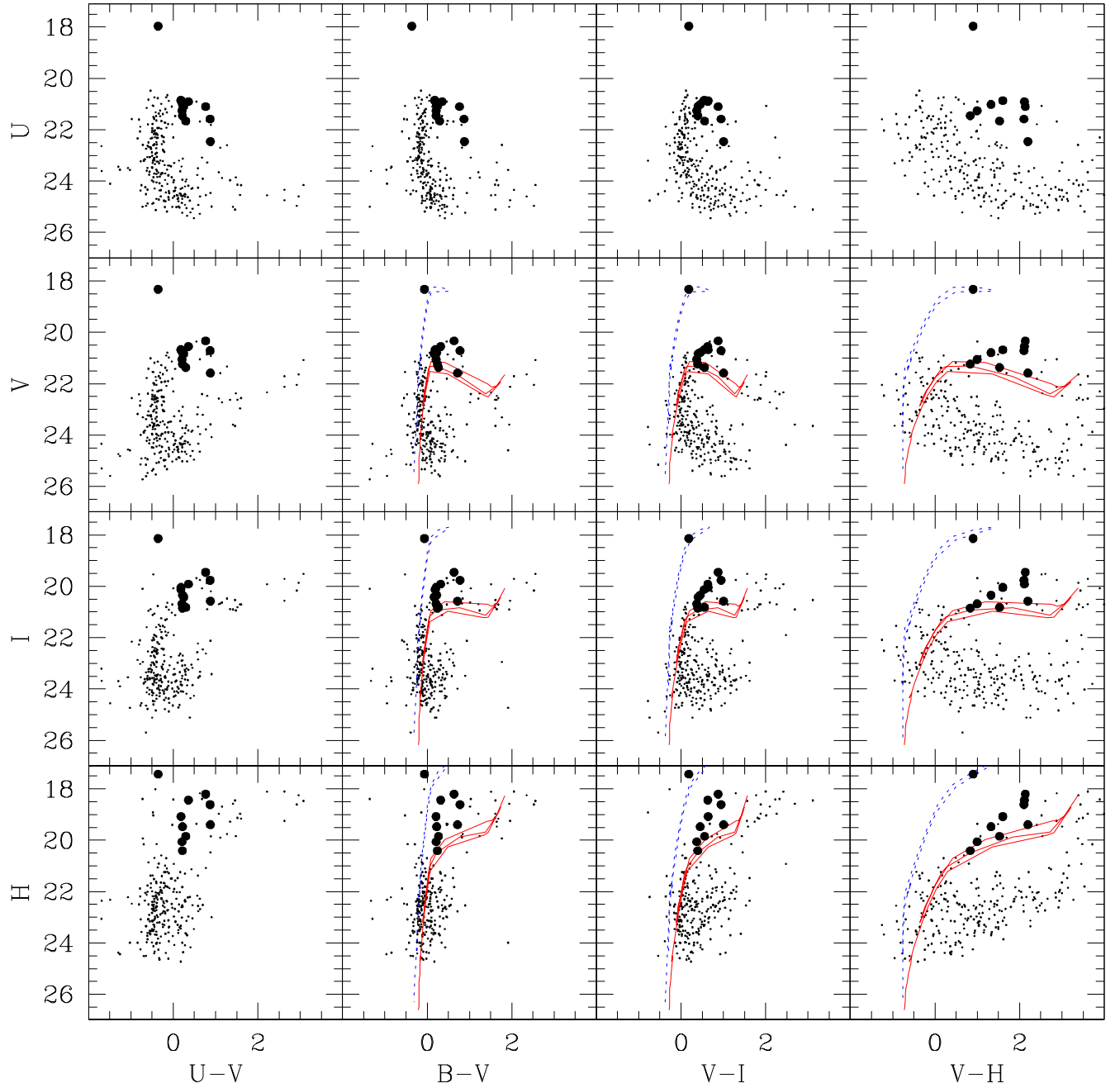


Fig. 3.— CMDs in different bands of the 256 objects with measured U, B, V, I, J, H magnitudes (calibrated in the HST-Vegamag system). Dots represent resolved stars and filled circles candidate clusters. The evolutionary tracks of a  $60M_{\odot}$  (dotted line) and of a  $15M_{\odot}$  (solid line) with  $Z=0.004$  (Fagotto et al. 1994b) are overplotted in nine panels.

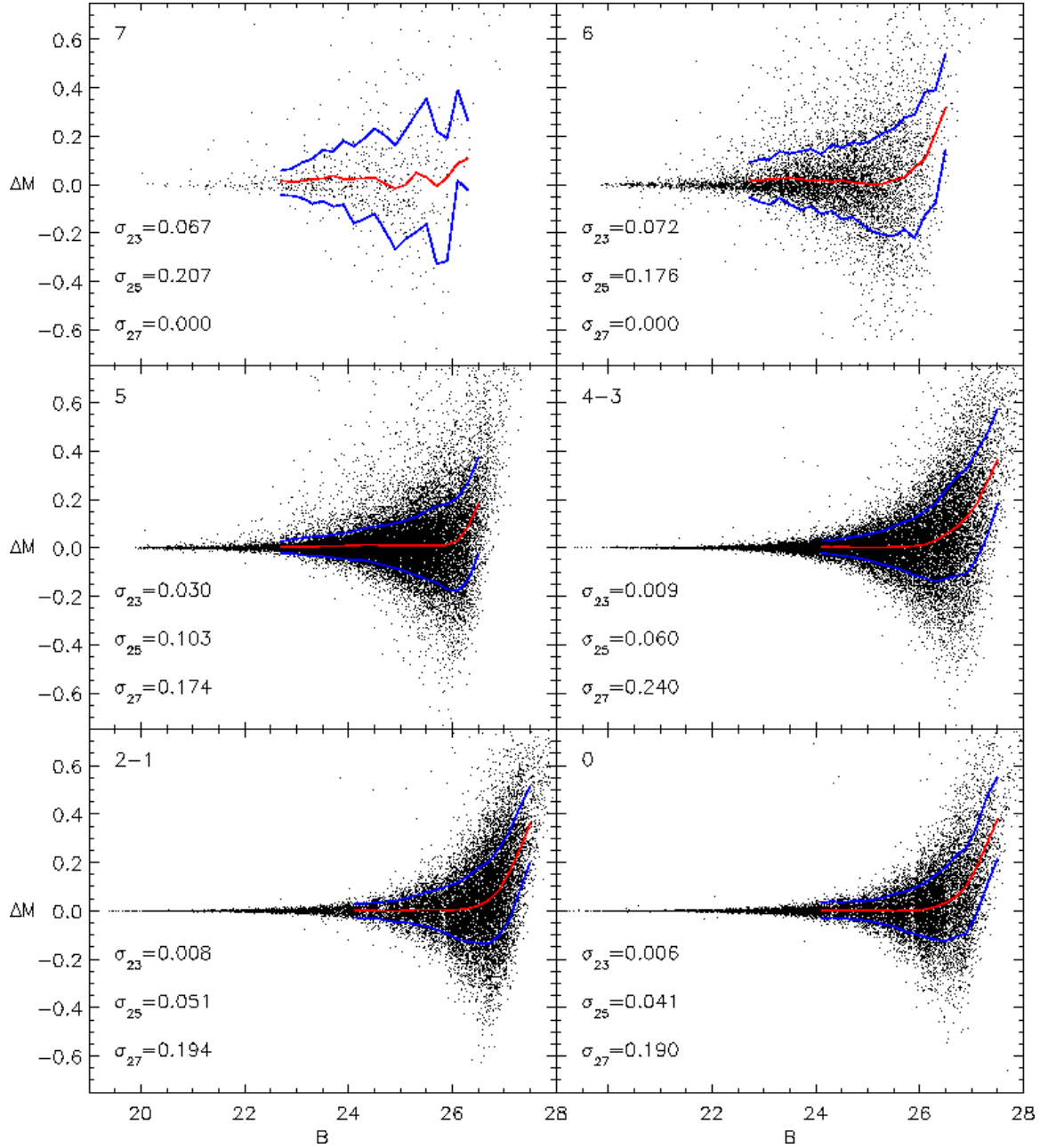


Fig. 4.— Magnitude difference ( $\Delta\text{mag} = \text{input} - \text{output}$ ) versus input magnitude in the HST-Vegamag B band of the artificial stars in the concentric regions. The standard deviations in 1 mag bins around  $B = 23$ , 25 and 27 are indicated for each region. The lines superimposed on the diagrams represent the local mean  $\Delta m$  and the  $\pm 1$  standard deviations.

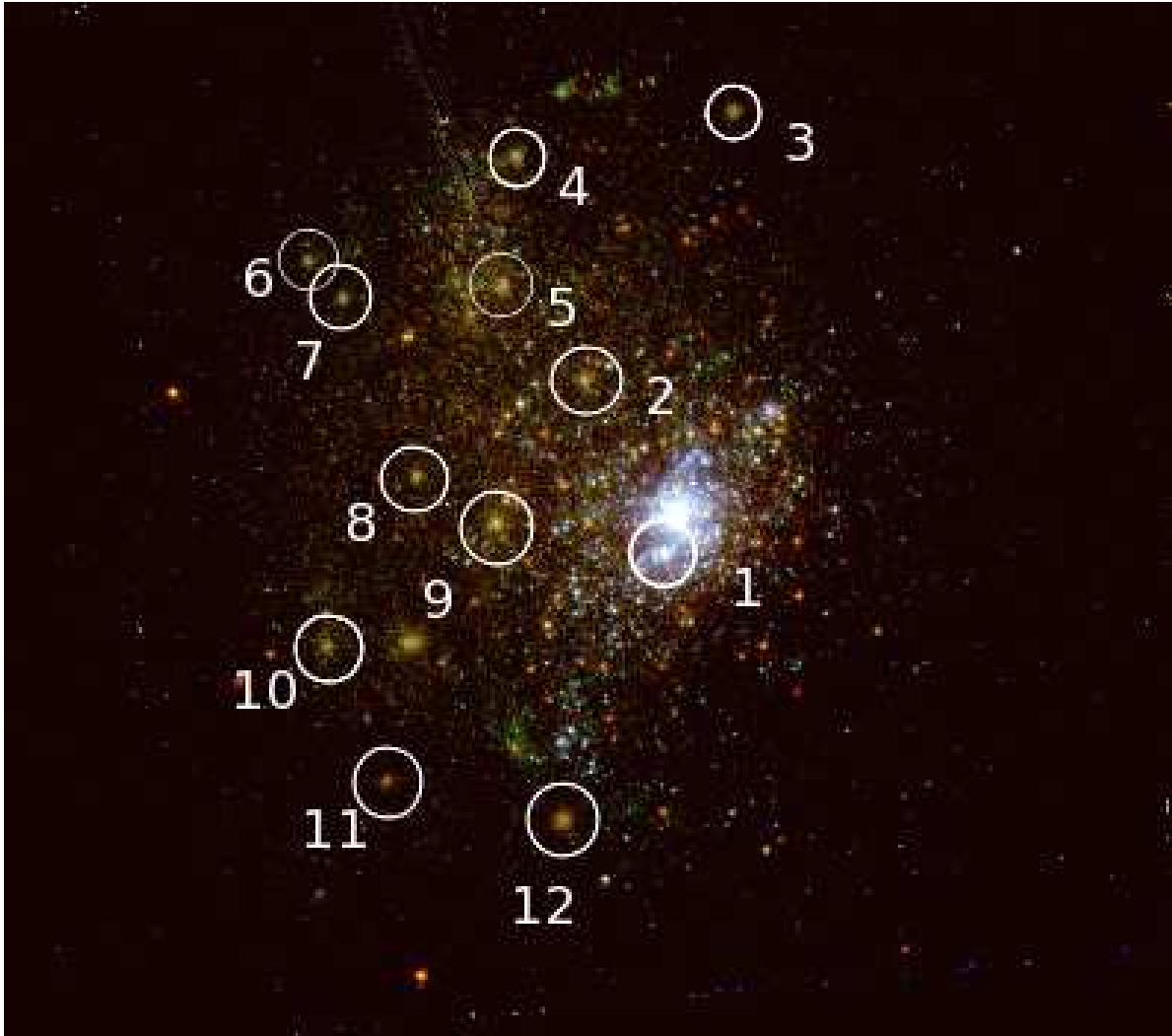


Fig. 5.— Three-color (F330W (U, blue), F555W (V, green), and F814W (I, red)) composite image of NGC 1705 obtained with ACS/HRC, showing a field of view of  $\approx 26 \times 29$  arcsec<sup>2</sup>. The selected candidate clusters are indicated on the image.

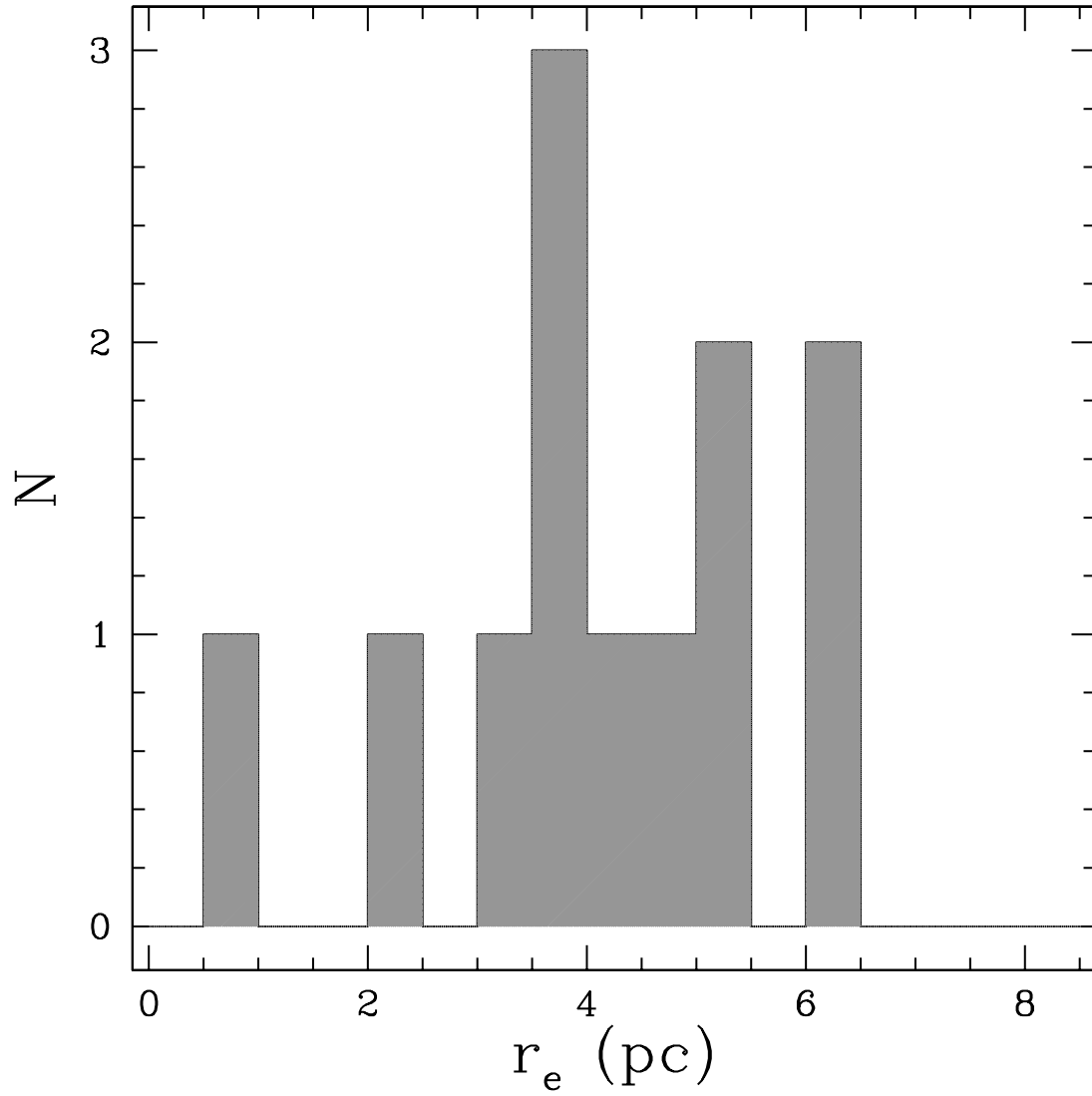


Fig. 6.— Intrinsic effective radius distribution of the 12 candidate star clusters from ACS/HRC data. A distance of 5.1 Mpc was adopted for NGC 1705.

nopagenumbers

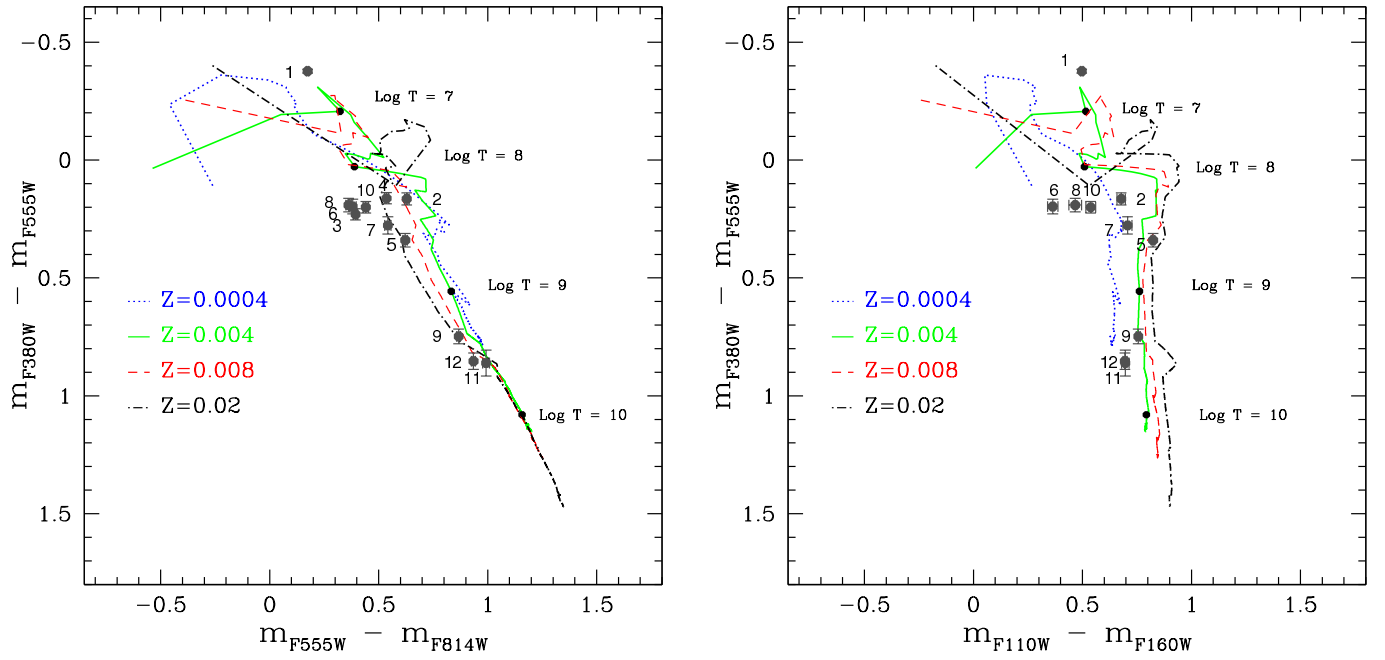


Fig. 7.— Left panel: U-V versus V-I diagram for the 12 selected candidate clusters. Right panel: U-V versus J-H diagram for the 10 clusters that have photometry in all the UBVIJH bands. The lines are the SSP GALEV models (Anders& Fritze-v. Alvensleben 2003) for different metallicities and ages from 4 Myr to 10 Gyr. The position of the  $\text{Log}(\text{age}(\text{yr}))=7,8,9,10$  models in the color-color plane is indicated by the black dots with the age labels for the metallicity  $Z=0.004$ . No intrinsic reddening was applied.

nopagenumbers

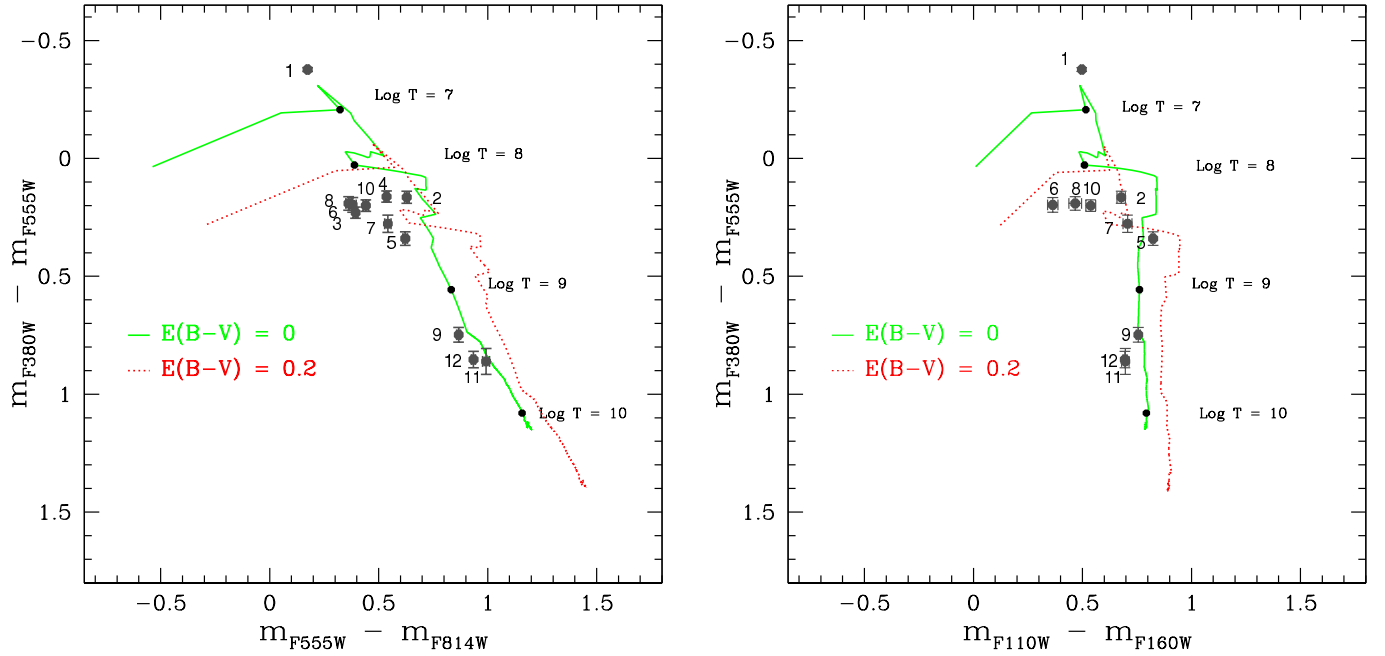


Fig. 8.— Left panel: U-V versus V-I diagram for the 12 selected candidate clusters. Right panel: U-V versus J-H diagram for the 10 clusters that have photometry in all the UBVIJH bands. The lines are the SSP GALEV models (Anders& Fritze-v. Alvensleben 2003) for a metallicity  $Z = 0.004$ ; the dotted one shows the effect of a reddening of  $E(B - V) = 0.2$  in combination with a Cardelli et al. (1989) law. The position of the  $\text{Log}(\text{age}(\text{yr})) = 7, 8, 9, 10$  models in the color-color plane is indicated by the black dots with the age labels for  $E(B - V) = 0$ .

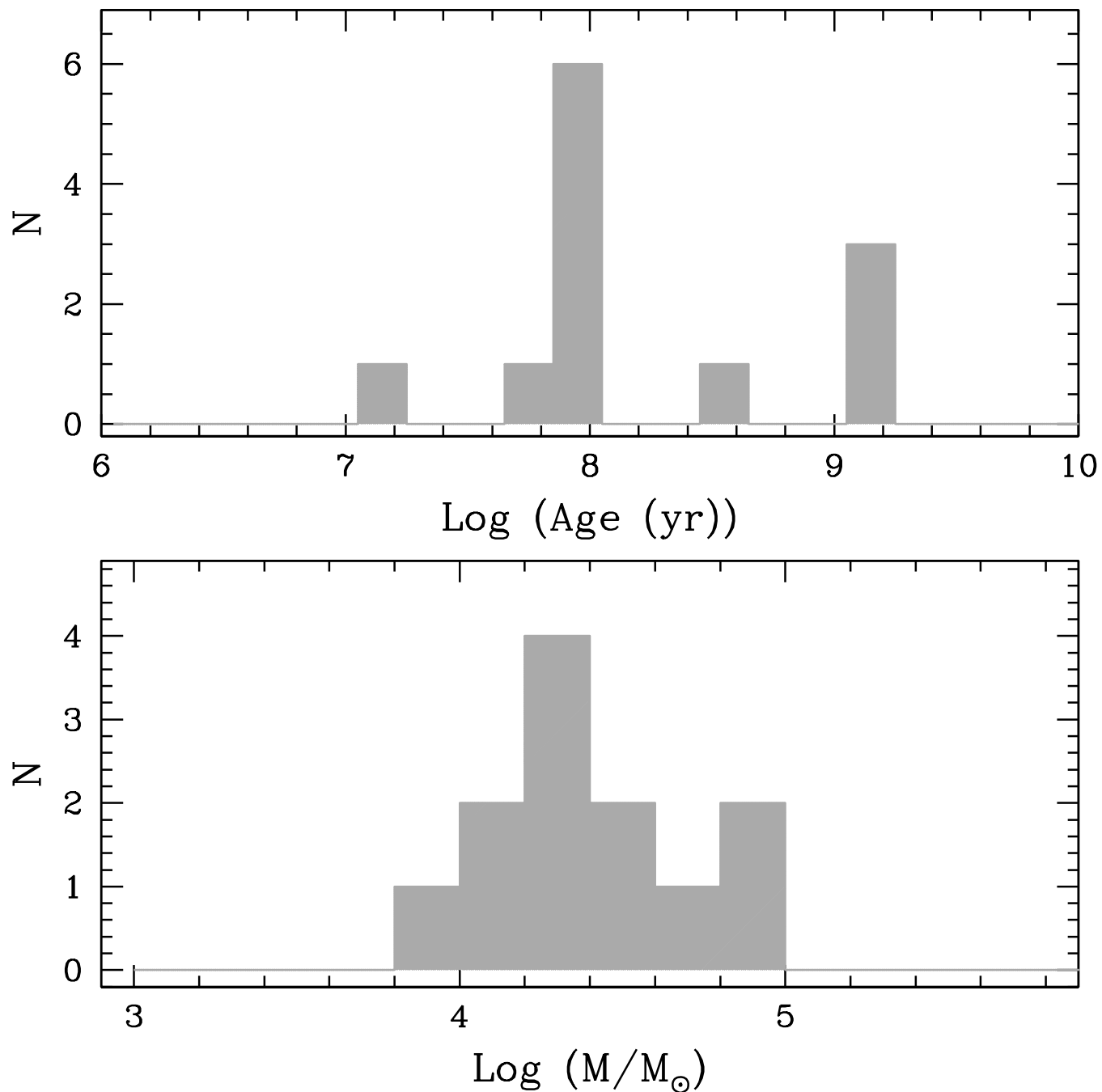


Fig. 9.— Age (top panel) and mass (bottom panel) distributions obtained for the 12 candidate star clusters by fitting the UBVIJH photometry with the GALEV models.

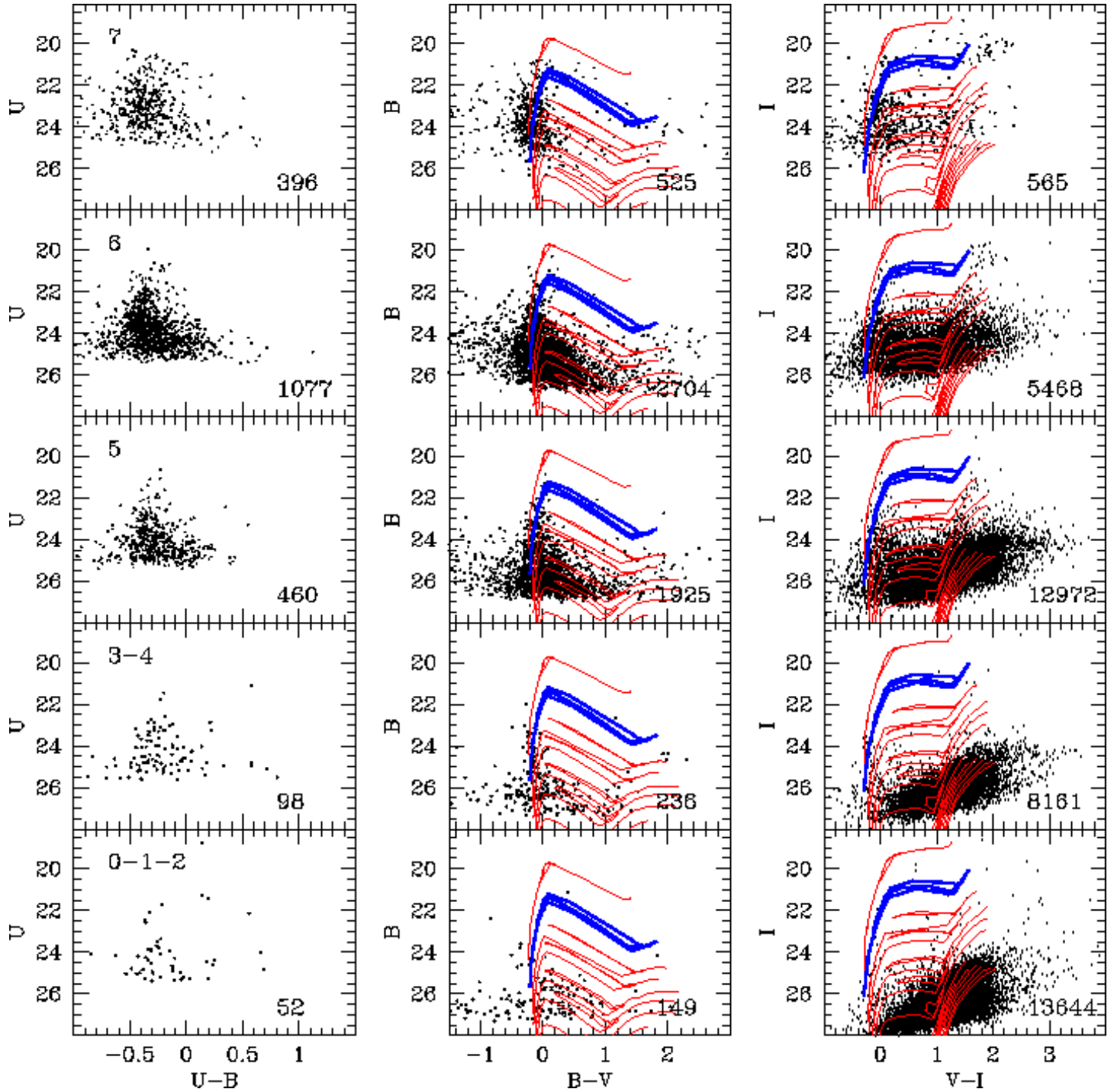


Fig. 10.— CMDs in the different colors of the concentric regions of NGC 1705 (labelled in the top-left corner of the left-hand panels). Magnitudes are in the HST-Vegamag system. Overimposed in the middle and right-hand panels are the Padova stellar evolution tracks for metallicity  $Z=0.004$  (Fagotto et al. 1994b) and masses from  $0.9$  to  $30 M_{\odot}$  (the displayed masses are  $30, 15, 9, 7, 5, 4, 3, 2, 1.8, 1.6, 1.4, 1.2, 1.0,$  and  $0.9 M_{\odot}$ ). The  $15 M_{\odot}$  track is plotted with the thick line. The number of stars in each CMD is indicated in the bottom-right corner.

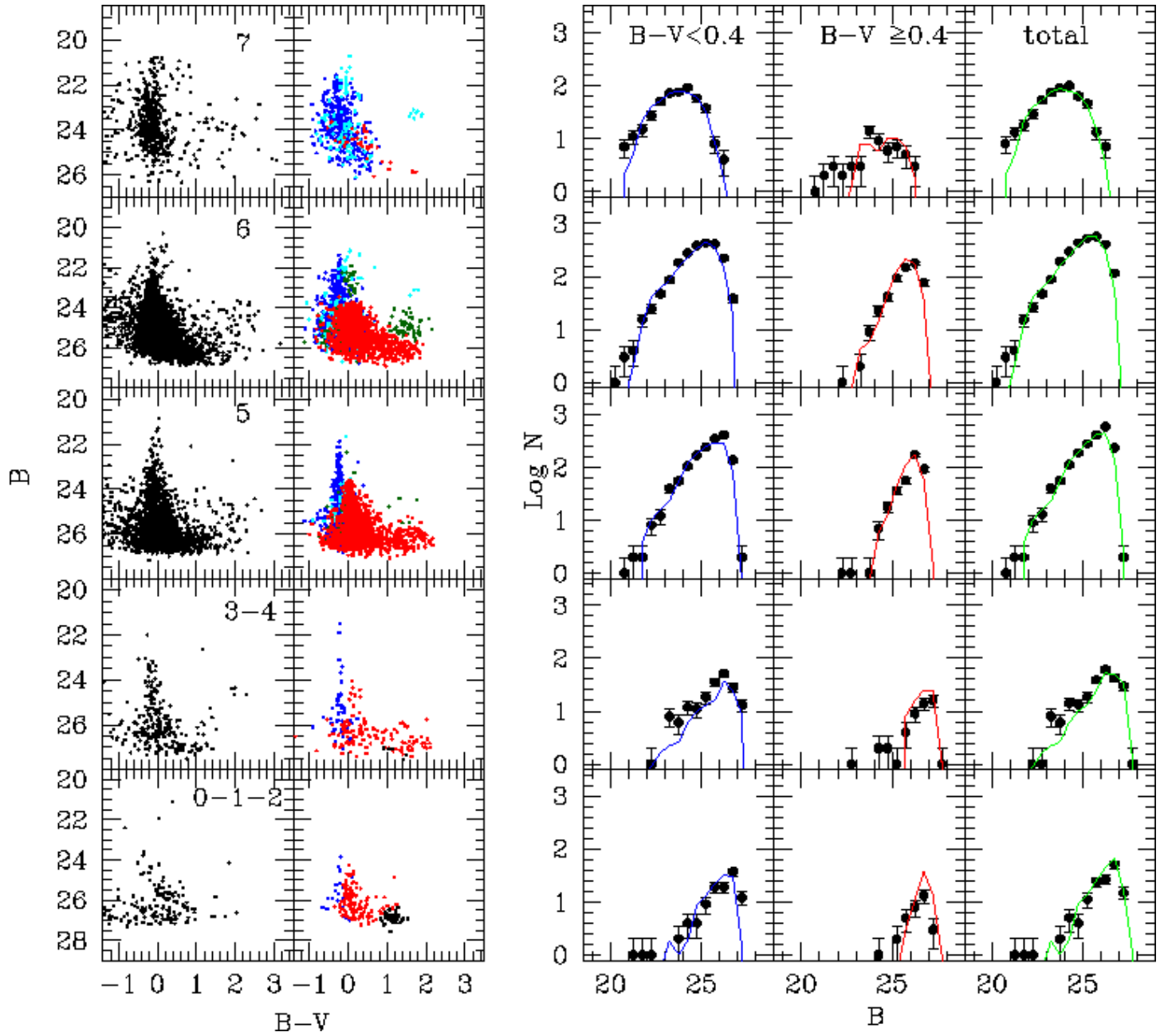


Fig. 11.— Comparison between  $B,V$  data and simulations. The observed  $B$  vs  $B-V$  CMDs (in the HST-Vegamag system) for different regions are displayed in the left-hand panels. Next to the observed CMDs, we display the synthetic ones obtained by assuming the SFH derived by A03, reported in Table 3. In the synthetic CMDs, the stars have been color-coded according to their age: blue = (0-3) Myr; cyan=(10-15) Myr; green=(15-50) Myr; red=(50-1000) Myr; black=(1-14) Gyr. On the right we display the LFs. Dots are for the data, continuous line for the simulations. From left to right, the LFs refer respectively to  $B-V \leq 0.4$ ,  $B-V > 0.4$  and to the entire color range.

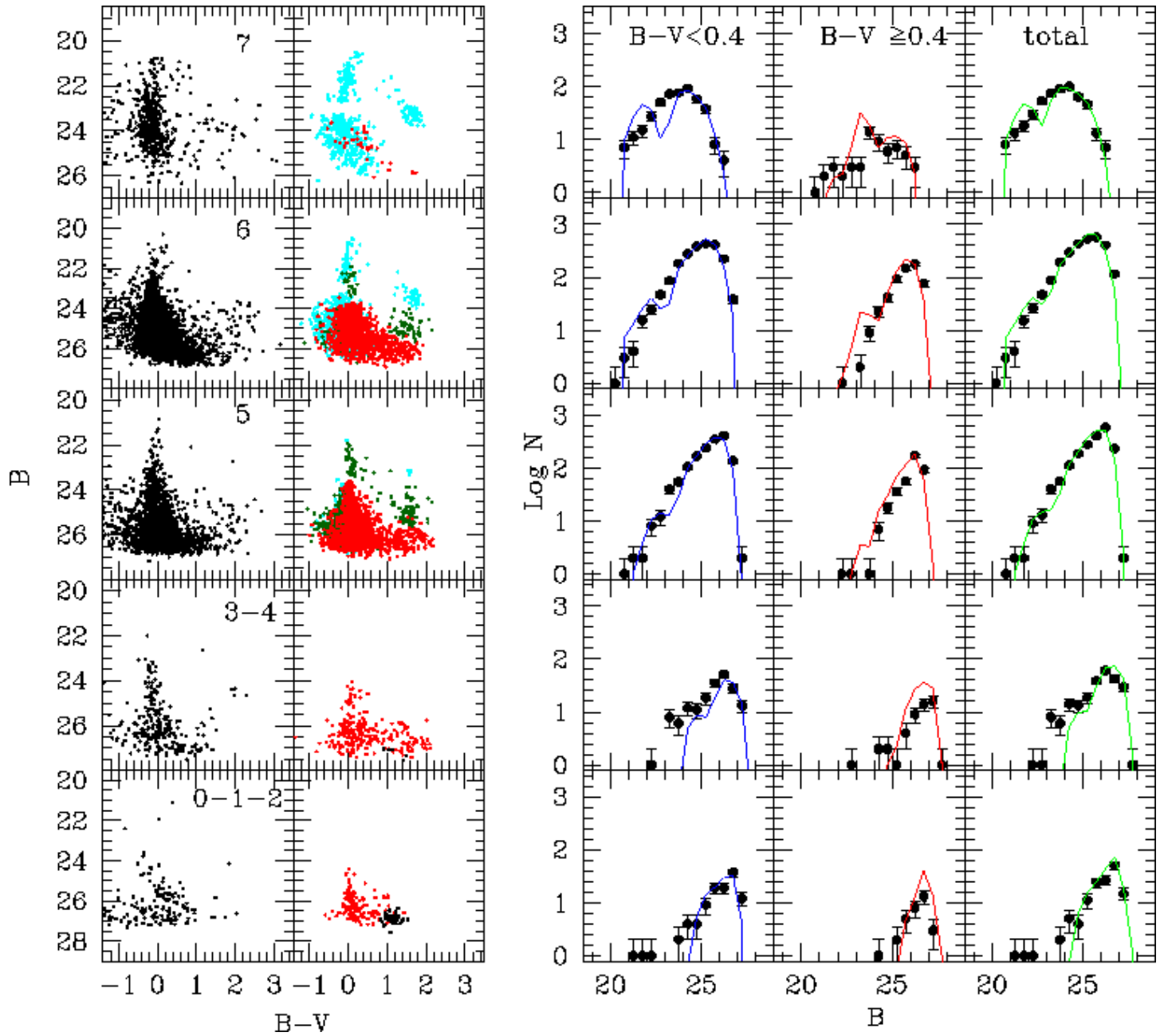


Fig. 12.— Synthetic CMDs obtained from the SFH of Tab. 3, but suppressing B2 (0-3 Myr). The stars of B2 have been re-distributed into B1 (10 -15 Myr). The color-coding is the same as in Fig. 11.

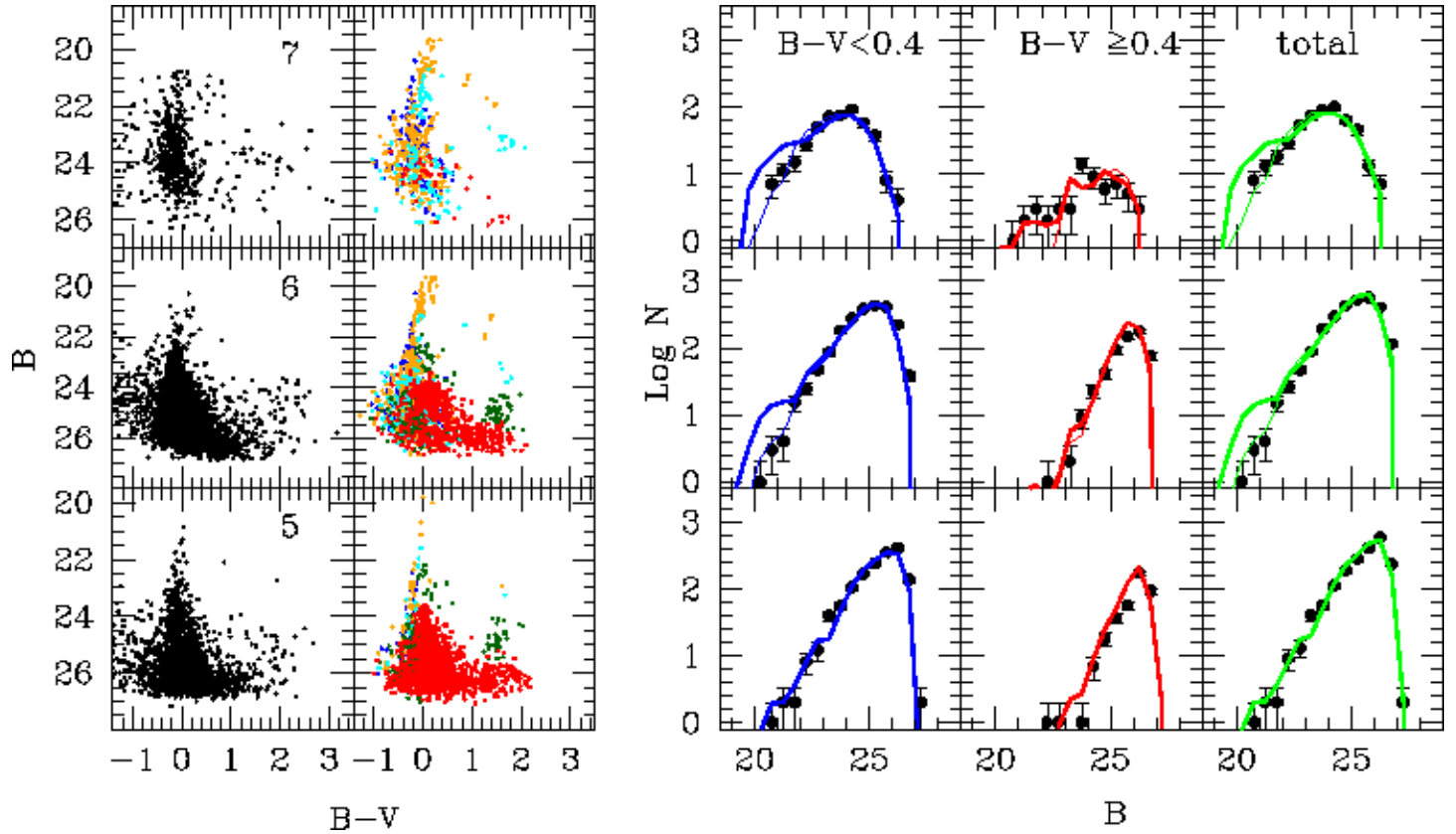
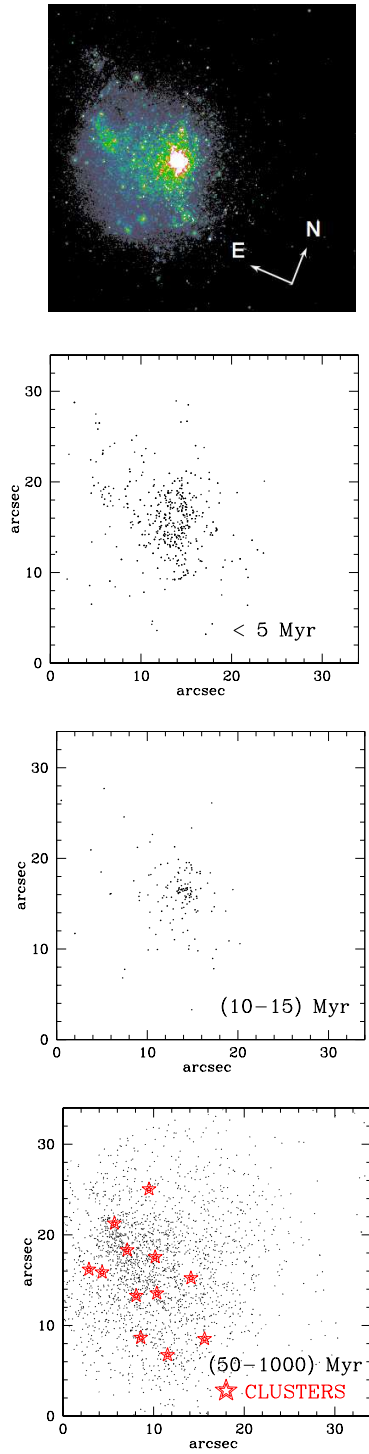


Fig. 13.— Synthetic CMDs obtained from the SFH of Tab. 3 but without quiescent interval between the two most recent bursts, and only for Regions 7, 6 and 5. From 15 Myr ago to now, the SFRs are  $5.3 \times 10^{-2}$ ,  $3.5 \times 10^{-2}$ , and  $6.3 \times 10^{-3} M_{\odot} \text{ yr}^{-1}$  for Regions 7, 6 and 5, respectively. The simulated LFs are plotted with a thick line. For Regions 7 and 6, we also display the LFs obtained assuming a rate of  $10^{-2} M_{\odot} \text{ yr}^{-1}$  in the last 15 Myr (thin line). The color-coding is the same as in Fig. 11, with the addition of orange dots for the stars with age (3-10) Myr. .



1

Fig. 14.— PC image of NGC 1705 in F439W (top) and spatial distribution of stars with different ages:  $\lesssim 5\text{ Myr}$ , (10-15) Myr, and (50-1000) Myr. The candidate clusters are overlotted on the resolved stars in the bottom panel.